Physically-based modeling of polymer foam microstructures: from realistic cellular microstructures and their variabilities to mechanical properties

T. Roland, Gaël Ginot, Mouhamadou Dabo, C. Gauthier, W. Drenckhan, P. Kékicheff

Physically-based modeling of polymeric foams microstructures: from realistic cellular microstructures and their variabilities to mechanical properties

T. Roland*[,a,b], G. Ginot[a], M.L. Dabo[a], C. Gauthier[a], W. Drenckhan[a], P. Kékicheff[a]

[a]Institut Charles Sadron, CNRS, Université de Strasbourg, 23 Rue du Lœss, 67034 Strasbourg

[b]INSA de Strasbourg, 24 Bld de la victoire, 67084 Strasbourg

* Corresponding author: thierry.roland@ics-cnrs.unistra.fr; thierry.roland@insa-strasbourg.fr

ABSTRACT

It is generally agreed that an efficient model for predicting the mechanical behavior of solid foams should present microstructural features similar to real ones. However, most theoretical results in foam micro-mechanics are based on periodic space-filling unit-cell which do not reflect the inherently random nature of real foams. The Kelvin cell or the Weaire-Phelan (WP) structure are by far the most used and yet they are only found is specialised foam. The present study therefore uses a versatile approach based on a thermodynamic description of interacting bubbles growth to produce representative volume elements of closed-cell foams with a wide variety of morphologies. Using a small set of parameters, one can build morphologies with local features specific to non-equilibrium foams. The behavior of the internal gas phase during the formation process is also modelled while assuming the absence of diffusion in the continuous medium. A sequence of mechanical micro-models is developed to study the complete compressive response ranging from the initial elastic response followed by the extensive plateau stress all the way up to the densification zone. The results are discussed in view of randomness of the cellular microstructure, anisotropic cell shapes effects and inner gas pressure effect. This is a major improvement over previous studies which lack variability in topological arrangement for 3D representative volume elements or which use periodic boundary conditions known to influence the way macroscopic instabilities develop.

Keywords: Foam material, mechanical behavior, randomness, numerical microstructures, modeling

I. Introduction

Cellular solids can be categorized into three fundamental structures [1]: honeycombs, open cell foams and closed cell foams. In an open cell foam type, the cells are interconnected like in a natural sponge, while closed cell foams consist of a set of gas bubbles separated by thin membranes of a solid phase. These microstructural features make closed cell foams widely used in many fields, such as transport, construction, and health, as they offer a good compromise between high modulus, strength and good energy absorbing capacity on one hand, and weight reduction and material savings on the other hand. Open cell foams have similar attributes but because of their high internal surface area, other functionalities include storage/filtering for chemicals or fuels [2] and porous scaffolds for bone in-growth [3].

It follows from their hierarchical microstructure that the mechanical properties of foams are governed by two major factors: the cell morphology (shape, size, positions, and their corresponding distribution) and the properties of the material constituting the foam. This was demonstrated by the pioneering works led by Ashby and Gibson [1] who described the macroscopic mechanical behavior of foam by using an analogy with a single cubic lattice that deforms either by bending or buckling. This analogy provides the right overall trends for the mechanical properties of the foam and highlights that the porosity is the main influential factor. However, this approach has put aside the complexity of the foam microstructure, thereby leaving open questions about the subtle interplay between the constitutive material and the hierarchical complex microstructure.

The widespread application of foams from home products to high-end technologies highlights the need of understanding the structure-property relationship for industrial and academic purposes. The main physical characteristics of the foam are dictated by its constituent material. Finer mechanical properties, e.g. elastic modulus, yielding and post-yielding behavior or acoustic or thermal insulation can be tuned through the cellular microstructure. Yet, determining the optimal arrangement and cell shape for optimized material performances at a given material density remains one of the most challenging questions in foam mechanics.

From a theoretical point of view, beyond the widely known survey by Gibson and Ashby [1], there are extensive works on the mechanics of open cell foams, but less on closed-cell foams. Relevant literature in the domain is given by Simone *et al.* [4, 5], Kraynik *et al.* [6-9] and Kyriakides *et al.* [10, 11]. These studies examined how the repartition of the solid material between the cells edges and faces affect the stiffness and the strength of metallic foams. In particular, the drainage phenomenon of the initially liquid matrix is a source of inhomogeneities

in the distribution of the continuous phase. If the excess liquid has no time to drain away sufficiently from the cell face to the adjacent cell edges before solidification, a local density gradient builds up leading to a high degree of material heterogeneity and anisotropy. This has repercussions on the mechanical properties since the foams deform mainly by bending and are therefore sensitive to the moment of inertia.

Most of these studies have considered foams of high porosity obtained through liquid state processes driven by interfacial tension. As a consequence, the approach relied on the minimization of the energy of a unit cell surface to describe the mechanics of foams with complex architectures. The Surface Evolver program initially developed by K. Brakke [12] to study surfaces shaped, among others, by surface tension and subjected to various constraints, has been extensively used for this purpose. One of the frequently used cell models is that of the periodic Kelvin cell model which is able to partition space into equal-volume units. It has very low surface energy and, accepting slightly curved edges, it verifies the Plateau's laws (1873) [13]. As an example, Zhu *et al.* [14] and Warren and Kraynik [8] studied the elastic response of a regular Kelvin cell at low and high compressive strains using beam theory. Interesting studies concern the influence on the stiffness response of cell face curvatures and corrugations [15], of cell shape variation [16] and of cell wall thickness variation [17]. All these studies emphasize the influence of imperfections (wavy cell walls, cell shape variations) or of the cross-sectional shape of the cell edges (Plateau border in comparison to circular or triangular shape) and they all conclude that it is necessary to incorporate the micro-geometrical details of the foam into the models to obtain valuable results. For instance, the stiffness is reported to decrease up to 40% of its original value when "wavy" cell walls (as opposed to "flat" cell walls) are considered in closed cell foams [15]. For open-cell foams having the same relative density, the Young's modulus was found to be 34% higher when the edge cross sections were modeled as Plateau borders in comparison to equilateral triangles [14]. This brief and not exhaustive literature review is concerned with mechanical properties for highly porous, mostly open cell foam types and arose from the minimized surface area approach for the geometrical characterization of the unit cell. However, a unit cell modeling approach cannot account for the non-periodic nature of the cell structures and other microstructural variations inherently present in real cellular materials. Also, the choice of unit cells respecting the basic rules for geometric stability given by Plateau (1873) is not the most appropriate: Kelvin or WP structure represent a minimal energy level that cellular materials cannot reach under standard manufacturing conditions [18]. Thus, Matzke noticed the absence of Kelvin cell in a dry foam [19] and Kraynik showed that foams exhibit topological disorder even when all the cells have the same volume

[20]. Because of the periodic boundary conditions (PBC), the mechanical properties measured in industrial foams differ from those predicted by idealized models for closed cell foams [21]. This overestimation even goes up to 50% for the compressive strength of metallic foams [1]. In the related literature, Voronoi tessellation is the principally used method to represent ordered or disordered structures of very low density closed cell foam, since they present similarity with real foams in appearance [22, 23]. However, one can regret the lack of studies based on large numbers of cells, the fact that they essentially focus on elastic properties, and that they are mostly 2D studies. In a general manner, a non-periodic arrangement of the cells leads to variability in the cell struts thicknesses which inevitably reduces the mechanical resistance of the structure through stress localizations. Grenestedt *et al.* [15] reported that disorder reduced the bulk modulus by 10% in comparison to Kelvin cell foams. With models composed of barely a few tens of cells, no prediction could be made regarding the mechanical behavior beyond the small deformation regime. The complete mechanical behavior depends on a combination of different microstructural fluctuations, e.g. varying cell sizes, curved cell walls, anisotropy, imperfections, which cannot be captured by repeated unit cells of classical geometry or by Voronoi tessellation. Also, as density increases, struts become thicker, joint regions become larger and eventually the approximations used to formulate beam theory cannot be applied anymore. In addition, two deformation mechanisms, namely edge bending and face stretching, occur simultaneously and cannot be treated in an uncorrelated manner. Therefore, no exact analytical prediction exists for the mechanical properties closed cell foams, requiring therefore extensive use of numerical methods. In particular, for a comprehensive description of the complex non-linear phenomena that occur at all length scales, a difficult issue is to accurately model the foam microstructure at a non-equilibrium state. This microstructural state is however abundantly (not to say exclusively) found within industrial products, and one of the ambitions of the present paper is to study to what extent the mechanical properties can be optimized thanks to microstructural variability offered by the current manufacturing processes. This question is very concrete for manufacturers who may be faced to microstructural defects induced by their manufacturing process or when they wish to optimize the properties.

For this purpose, our previously developed “ad-hoc” modeling method used with success to generate a wide range of realistic closed-cell foam is retrieved and generalized in this work [24]. Based on a simplified physical description of a gas-releasing foaming process, our numerical method allows to simulate structures with characteristic microstructural imperfections inherent to most real cellular materials. It provides access to relevant ranges of microstructural variability to be considered simultaneously which is not usual in the literature.

The first section of this paper describes the numerical method briefly and shows how to obtain representative numerical foam microstructures for wide range of order/disorder and densities. In a second part, a quantitative description of the morphology is proposed for the numerical foams. This description is supplemented with a structural description of the foams, based on the spatial organization of the bubbles and the location of their physical contacts. This analysis is led *ab initio*, using an external, home-made reconstruction algorithm developed to study the structures of the foams and emulsions. In a third part, the mechanical properties are studied with a particular emphasis on the non-linear behavior related to morphological characteristics such as a non-uniform and disordered cell structure. Since most models in the literature consider the role of the gas to be negligible, except the works done by N.J. Mills [25], we incorporate it in our models to check the limit of the validity of this assumption. The results are interpreted and analyzed in relation to the ones published for very low density closed cell foams when they exist. It turns out that while the elastic behavior of closed cell foam is only marginally affected by the morphology of the microstructure in the considered density range, the effect is much more pronounced for large deformations. The main trends of the mechanical behavior are given in relation to the microstructural features defined by statistical parameters. The presented results can help for the design of the foams and especially for the choice of morphology in order to reach a certain level of performance. At last, a comprehensive understanding of possible mechanical instabilities and their non-linear effects during deformation of closed cell foam is given. In this way, a scheme is specified to predict the mechanical instability of foams based on their morphological features.

II. Materials and methods

II.1. Modelling of 3D cell foam-like microstructures

The main challenge when considering micromechanical modelling of closed-cell foams is to properly approximate the foam microstructures, which are fairly irregular and random, and highly dependent on the density level. In most cases, the cellular solids result from the nucleation and growth of multiple cells. If all cells are considered to nucleate simultaneously in space and grow at the same rate, then a set of spheres may serve to describe low porous cellular materials while a Voronoi diagram will be better suited for high porosities. Accordingly, crystallographic arrangements, random close packing (RCP) methods [26] or even random sequential adsorption (RSA) algorithms [27] have been used to investigate low porous cellular materials for which gas bubbles tend to pack in the closest way. When the

volume fraction of the discrete phase is approaching the "touching limit" or jamming fraction φ_d^*, the need for different geometrical representative units arises, as gas bubbles may interact, deform, and eventually coalesce. The spherical shape can no longer be conserved. The Voronoi tessellation of the space is fully determined by the initial locations of the generating seeds, also named nucleation points. Perturbations in the locations of evenly spaced seed points allow to generate irregular cell shapes, with variations in cell wall thickness [7-10, 14-17]. Although Voronoi-based models can provide important results, they are limited in their ability to account for the type of microstructural imperfections inherent in foaming processes. Here, the focus is on industrial polymeric closed cell foams of medium to high porosity for which cell shapes are neither fully spherical nor fully polyhedral. These foams are usually obtained from the gas release of blowing agents (CBA) after chemical reactions or evaporation (usually such as CO_2 or cyclopentane). These foaming processes are quite different from that of soap foams as the rapidly changing viscoelastic nature of the molten polymer combines with the surface tension to give the final foam microstructure. Some studies have even shown that the contribution of the interfacial tension is negligible compared to the viscous stresses arising during the expansion phase of a polymer foam [28-34]. In addition, available numerical studies of soap foams have focused on the evolution of the structure towards an equilibrium state in the absence of expansion, since the simulated foam evolution takes place at constant gas volume. In this case, the transition to an equilibrium state is driven by local topological changes in the structure driven by surface area minimization. Thus, in the present study, we chose a different modeling approach which distinguishes from previously published work by focusing on the numerical representation of foam microstructures in a non-equilibrium state with all their complexity, as close as possible to real ones. Our modeling approach is described in detail in reference [24]. Here, we only provide some of its key features to allow the reader to follow the progress of the study. The current *ad-hoc* modeling method is inspired by the physical basis governing the formation and expansion of gas pores in a polymer melt. As such, one is capable to simulate the evolution of interacting bubbles in a polymer melt encompassing all the steps from the nucleation stage (where tiny closed-cells form) to their expansion and maturation until the ultimate microstructure is reached.

During the expansion stage, the motion of an elementary particle (material element) is described by the Navier-Stokes equation considering the radial fluid flow of the polymer mixture. This one is defined as an evanescent spherical wave whose magnitude depends on the principal viscoelastic characteristics of the mixture, in particular, its dynamic viscosity η_T, its bulk elastic modulus K_T, and its density ρ, all depending on temperature T. Accordingly, one

may infer the main influence of the rheology on the morphology and structure of the ultimate polymer foam. At the gas-melt interface, for each individual cell, in addition to the reaction forces in the polymer melt, the interacting forces generated by the internal pressure in the cell and the force arising from the interfacial tension are considered. Thus, one of the main focuses of the *ad-hoc* model relates to the interactions between the bubbles that grow and deform while they approach and encounter neighboring ones to ultimately lead to the complex microstructure of the foam. While currently available method based on Voronoi tessellation considers a constant growth rate, here, the cell growth rate is limited not only by the rheology of the polymer, but also by the temperature and the pressure of the system, the time allowed for the cells to grow before solidification, and the presence of other bubbles. In this sense, the *ad-hoc* modeling method appears advantageous as it is a more dynamic approach combining the radial flow of the mixture while the cells nucleate and grow at the same time, together with the gaseous release. Concerning the cell nucleation, a configurable temporal and spatial distribution is available so that different scenarios inherent to a given foaming process can be produced. The number of cells is given by a nucleation time distribution which defines a nucleation rate while the locations of their centers are determined according to a random selection algorithm which allows both homogeneous and heterogeneous nucleation to be modelled. These terms refer to simultaneous nucleation of cells or not, leading ultimately to monodisperse or polydisperse structures, respectively. The heterogeneous nucleation is usually more favorable when several additives or organic charges are employed as they constitute nucleation sites during the polymer foaming processes [33].

The validity of the present physically based model to generate numerical microstructures that mimic real foam microstructures was demonstrated in ref [24, 35]. In particular, it was demonstrated how polydisperse polymeric solid foams can be generated, and how close their ultimate morphology resembles the real ones as investigated by high-resolution X-ray microtomography using synchrotron radiation. Since the Surface Evolver and other Voronoi tessellations are difficult to adapt to foams of medium to high density where non equilibrium microstructures are set, our physical modeling method appears advantageous for generating such microstructures and for a subsequent investigation of their mechanical properties. By these aspects, our work distinguishes itself from previously published investigations, which are either based on minimizing the surface energy or where a spherical shape is assumed for the whole expansion modeling. In the latter, it is usually proposed homogeneously distributed nuclei, a known growth rate, no interfacial tension effects during cell growth and no multi-cell wall interaction. Thus, the attainable porosity range is rather

limited. And this limitation is quite frustrating considering that applications require foams with a large range of porosities. Thus, foams of medium porosity are used in static sealing, vibration reduction or structural reinforcements for car bodies and aerospace vehicles. For example, elastomeric closed cell foams with porosity of the order of 60% are used for their good anti-vibration properties in the transport industry. Or, epoxy-based closed cell foams with porosities in between 40%-60% are used as crash absorbing elements in the automotive industry. The practical interest in the study of their mechanical performances, e.g. for industrialists, translates in specific structural considerations, such as the variance in elastic properties introduced by variability in the arrangement of cell wall, or the differences in elastic properties between isotropic and anisotropic microstructures. These two sources of variability are commonly used by industrialists in the field: by adapting different thermal paths from the CBA process, deferred nucleation occurs and a certain polydispersity is attainable, by adjusting the homogeneity of the native chemical compounds mixture of the foam, a more or less random distribution of cells is possible and finally the use of specific mold is well known to promote directional growth. Note that a simultaneous nucleation of randomly distributed cells will inevitably lead to a multi-size structure (polydisperse).

Our study adopts a 3D regular structure based on the face centered cubic lattice (FCC), which is more representative of the foam structure than the simple cubic structure [36]. To adapt this cell configuration, all the cells were nucleated at the same time from their FCC location. For the cell growth generated by the *ad-hoc* modeling method, the viscoelastic parameters of the polymer melt and the surface tension were the ones specified in the reference [24]. Then, a method of finite perturbation [37, 38] of these regular sites was performed with the purpose of modeling irregular cellular solids with non-uniform cell shapes. Figure 1 gives an illustration of the perturbation method to generate random structures using, for the sake of illustration, a Voronoi diagram to represent the spatial partitions occupied by the points of the structure. From the initial regular distribution of a given set of points M_i, the parameter α gives a different distribution by moving all the points according to $\alpha l_0 \vec{U}_i$ where l_0 is the mesh parameter of the initial regular distribution, $\vec{U}_i$ is a unitary vector randomly oriented from the point M_i and α is a dimensionless value between 0 and 0.5. The α parameter characterizes the degree of perturbation: the higher the value is, the more disordered the structure is.

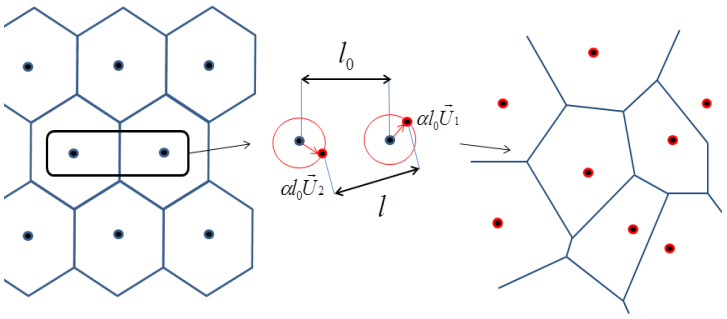

Fig. 1. Setting of the spatial distribution of cell seeds: l_0 seed inter-distance at initial regular state, l seed inter-distance after perturbation applied through random vector $\vec{U}$ with magnitude α.

To analyze the sole effect of disorder on the mechanical properties of the foam, we took care to keep the same porosity between the models. This porosity was chosen to be 62%, a value representative of foams frequently used in car bodies reinforcement and vibration reduction.

Figure 2 shows the 3D microstructures numerically generated by varying the α parameter only, the other parameters of distributions as well as the porosity being identical between the models. Each specimen includes about 800 cells and will serve as templates for calculating the foam mechanical behaviors via finite element modeling. The time to run a foaming simulation on a standard desktop PC depends on the size of the grid: it takes typically few hours to generate a few tens of cells, but more than two days for one thousand cells.

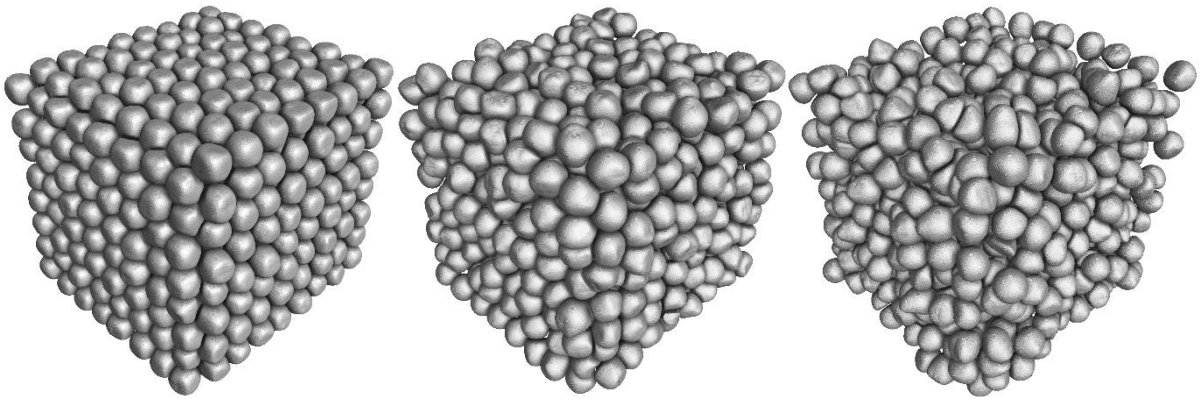

Fig. 2. 3D foam-like microstructures generated by perturbing the central positions of an FCC crystal using $\alpha=0^+$(left); $\alpha=0.2$(middle) and $\alpha=0.3$ (right).

II.2. Finite element models and computation

The output of the *ad-hoc* modeling is a DXF or STL file containing all the mesh nodes describing the numerically generated foam structure. The surface contours are then realized by surface patch arrangements replacing the initial mesh. At last, the volume mesh is obtained by

an intersection geometric operation between these cells and any solid contour. The finite element program (FE) used for subsequent mechanical analysis is MSC Marc. This FE program includes toolboxes from experimental data fitting to several material models and it is able to interpret scripting language as Python allowing automated procedures to be generated. 4-node tetrahedral elements are chosen for the meshing of the foam structure. Attempts to use higher interpolation through mid-nodes to the tetra-elements lead not only to a prohibitive computational cost but also to some convergence problems that arise from an increased sensitivity to any mesh distortion. Prior to run the simulation, a mesh quality check was performed. In particular, we verified to have sufficient mesh elements through the wall thickness to avoid undesirable effects such as volumetric and shear locking. It was found that a minimum of two elements per thickness is required to reach mesh convergence.

The constitutive material chosen for the base material is a bilinear isotropic hardening material. The material parameters are inferred from tensile/compressive stress-strain profile measured by us on a bulk thermoplastic polymer (not foamed) commonly used in foam industry. A Young's modulus of 10 MPa is obtained and a Poisson's ratio of 0.4. A plastic flow criterion based on von Mises is adopted, with a yield stress of 2 MPa. Finally, it turned out that a model containing 600 cells is a representative volume element (RVE). The size of this RVE was carefully established in our previous study [35] and respects the required ratio of the specimen size to cell size equaling to ~6 [39, 40]. In comparison, 2D studies of the foam stiffness were shown to be relatively insensitive to the RVE size and only a few tens of cells may be used. The use of a few hundred cells is more appropriate to account for the dynamic response [41] and for the large-strain compressive behavior [37, 38]. In 3D, less than twenty cells were used by Grenestedt *et al.* [16] for investigating the effect of cell shape variations on the elastic stiffness of closed-cell foams and one hundred cells constituted the RVE for elastic moduli analysis of random models based on Voronoi tessellations [22]. At last, for large strain analysis of 3D random closed cell foam structure, 125 cells were used as RVE [42]. Comparatively, 216 cells were chosen as RVE [43] but up to 700 cells when morphological details were sought [44, 45]. By using a sufficiently fine mesh to ensure that the thinnest and most curved cell walls are correctly described, a standard model typically contains between $1.5.10^6$ and 2.10^6 elements, thereby asking for about 120h of CPU time using a workstation @ 3.5 GHz with 128 GB RAM.

The link between the non-linear part of the response at large compressive strain and the inner structure of the foam (with all its variabilities) being the focus of the present work, the option for a self-contact detection was used for the finite element model. Displacement boundary conditions were imposed using an infinite rigid top plate while a fixed bottom plate

acts as a support. Frictional effects were accounted for between the plates and the foam material to prevent any sliding during compression. However, no friction coefficient was set for internal contact between the cell walls, i.e. when cell walls come into contact with each other during compression. To consider the gas contribution, closed cavities were defined by selecting the element faces forming the cells. This option is available in MSC Marc, however a python procedure was written to automate the detection of element faces for the numerous cell cavities and assign the gas properties to them. The gas was assumed to be ideal with a fixed mass and at initial pressure P_0 of one atmosphere. In most polymer foams air diffusion over weeks of storage means that P_0 is equal to the atmospheric pressure. For a better stability of the FEM results, an iterative approach was invoked through the cavity parameter instead of the default incremental approach. This means that the cavity volumes are updated at every iteration rather than only at the end of the increment.

Ad-hoc microstructural models are non-periodic just like real foam microstructures. This precludes the use of periodic boundary conditions (PBC), unless modifications or specialized methods, as the ones presented in [46] or [47] were done. As a result, the outer surface of the numerical foam sample is not constrained in lateral directions. Usually, this requires a large enough sample to avoid any border effects, but it avoids artificially stiffer response known to be produced by PBC [48]. Indeed, PBCs tend to interfere with the mechanisms of microstructural instabilities by constraining lateral displacements.

II.3. Morphostructural analysis

The structure is reconstructed from the vector images resulting from the *ad hoc* simulations (stack of horizontal slices) using a home-made reconstruction algorithm [49] developed to study the structure of foams and emulsions. Numerically generated bubbles are already separated by medium voxels, and thus do not require a segmentation step. Individual bubbles are labelled using the *segmentation.random_walker* function from the Skimage library. The voxels included in every bubble are given a value corresponding to their label. The voxel positions of their interfaces are detected using the *measure.label function* of the same library. The positions of their centroids are computed as the average positions of their voxels. The labels, the positions of the centroids and of the contour voxels are stored in separate csv files and are then used to detect the contacts or the distance between the nearest neighboring bubbles.

The distance between two bubbles is defined as the separation between their surfaces (Surface-to-Surface or S2S distance) as shown in Fig. 3. For this calculation, the computation is limited to physically relevant voxels by selecting the ones that are on the contours and inside

a cylinder of radius of 20 voxels length joining the two centroids (red zones on bubble surfaces on the left of Fig. 3). Among this set, the smallest distance is taken as the surface-to-surface distance and used to determine the "contact relations". Two bubbles are considered to be "in contact" when their S2S distance becomes smaller than a user-defined distance threshold d_{thresh}.

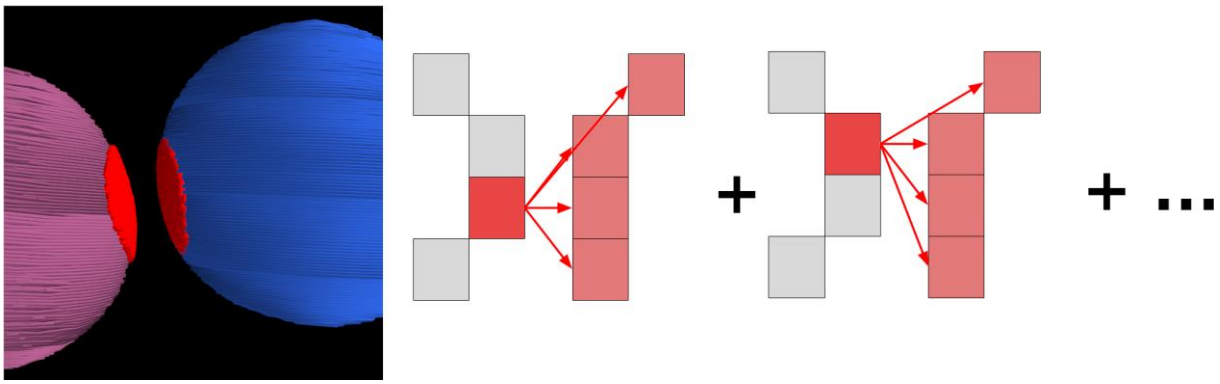

Fig. 3. (Left) preselection of the voxels between which the distances are computed. (Right) the distances between each pair of voxels from different cells are computed iteratively.

The radial correlation function is computed following standard procedures, through an average over every bubble. To limit the effects of sample borders, we restrict the set of bubbles used for averaging by removing the bubbles that are outside the box of total volume shrunk by 15% in every direction, as shown in Fig. 4. The extension of the shell is stopped once the first neighbor outside of this box is encountered. The bond orientational order parameters q_4, q_6 are computed using the pyboo library [50]. The Shannon entropy per bubble is computed following the procedure described by Brujic *et al.* [51] : A random position is taken inside the contact network, and a sphere is grown until a contact network of n bubbles is obtained inside this sphere. The class f of the graph is computed by extracting its set of automorphisms using *pynauty*. This operation is repeated 800 times to obtain a probability distribution of the classes $P(f)$. The Shannon entropy of a graph of size n is calculated as $H(n) = -\sum i\, P(f_i) ln(P(f_i))$, and the entropy per bubble is taken as the slope of $H(n)$ in the linear regime with n to limit the border effects.

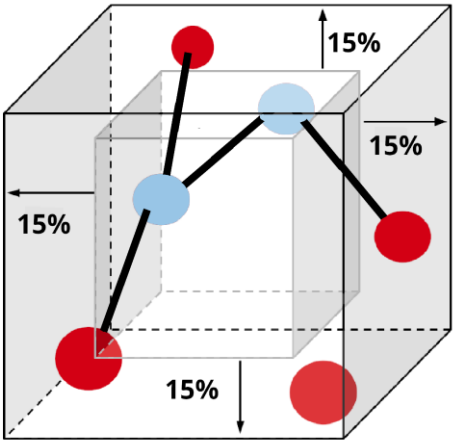

Fig. 4. The number of contacts of a particle is taken in account in the average only if its centroid is inside a subvolume, delimited by shrinking the bounding box by 15 % in every direction. The contacts with bubbles outside the subvolume are preserved and counted to obtain < Z >.

III. Results and discussion

III.1. Structure and morphology

To obtain insight into the effect of a random cell organization on the compressive behavior of foams, three degrees of perturbation were investigated. The parameter α was initially set to $\alpha = 0^+$ to describe nearly perfectly periodic foams and was then increased to α = 0.2 and 0.3, while keeping the relative density ($\bar{\rho} = 1 - porosity$) at the constant value of about 0.38, representative of commercial PVC foams. It has been noted that for real foams, the identification parameters used in the generation of the foams may not be sufficient (e.g. impact of the shape of the cells, correlations between the distributions) to uniquely characterize the morphology of their microstructure: the local neighbourhood relations, the geometrical and topological local organizations, the deformations of the bubbles and the correlations over length scales larger than the bubble size are all important features of the foam structure impacting its mechanical behavior [52-55]. Therefore, in a first section, the morphometry of the foams is presented through cell sizes, shapes and wall thicknesses. In particular, the cell size distribution is identified through a dimensionless ratio C_{vol} of the standard deviation over the average volume of the cells ($C_{vol} = \frac{\sigma_{vol}}{<vol>}$). Similarly, the deviation from the spherical character is described through its C_{sph} coefficient for the dispersion. Then, one can apprehend the structure of the foams through the geometrical and topological organizations of the cells. This analysis is performed using a home-made segmentation and characterization algorithm taking as input

the horizontal slices of the foams, as provided by standard tomographic imaging setups. The code is made freely available online for the interested users[1].

To insure the uniqueness of the results, a reproducibility analysis of our *ad-hoc* numerical foam generator had been already proposed [24]. Two simulations run with the same input parameters (thus leading to a same porosity and C_{vol}) gave microstructural models with the same compressive response. However, for the more polydisperse structure, some small differences could be noted at large deformation. It will be seen later that the behavior at large deformation is very sensitive to the two parameters which characterize the heterogeneity of the microstructure: a slight difference either in the values of α or C_{vol} can generate small deviations in their mechanical responses. Such conclusion was already noted in our investigation of the 2D case [35].

Figures 5 and 6 represent the metrics used to characterize the morphology of the final microstructures. These analyses are based on 830 cells for varying degrees of randomness α. The cell size is determined from the relative cell volume distribution and the equivalent cell diameter D_{eq}. The sphericity parameter S_{ph} is used as a metric of the anisotropy of the cells, counted as a deviation from a perfectly spherical shape. It is defined as:

$$S_{\mathrm{ph}} = \frac{\pi^{\frac{1}{3}}(6V)^{\frac{2}{3}}}{S} \qquad Eq.\ (1)$$

where V is the volume of the cell and S its surface area. The sphericity has a maximum value of 1, which corresponds to a perfect sphere. The sphericity depends on both form and roundness of the cells [56]; for instance, the sphericity of a cube is 0.80 whereas that of a hemisphere is 0.84. Since the cell shapes of the studied structures are not very angular and are of similar roundness, the sphericity reflects an anisotropy through an elongation of the shape. The thicknesses of the cell walls were measured using a maximal inscribed spheres method [57] directly applied on the vector images resulting from the *ad hoc* simulations. Compared to the previous S2S measurement, it is the distance distribution between neighboring cells which is obtained. The distribution of the wall thickness is shown in Fig. 6.

[1]https://github.com/SimianLibrarian/vritra

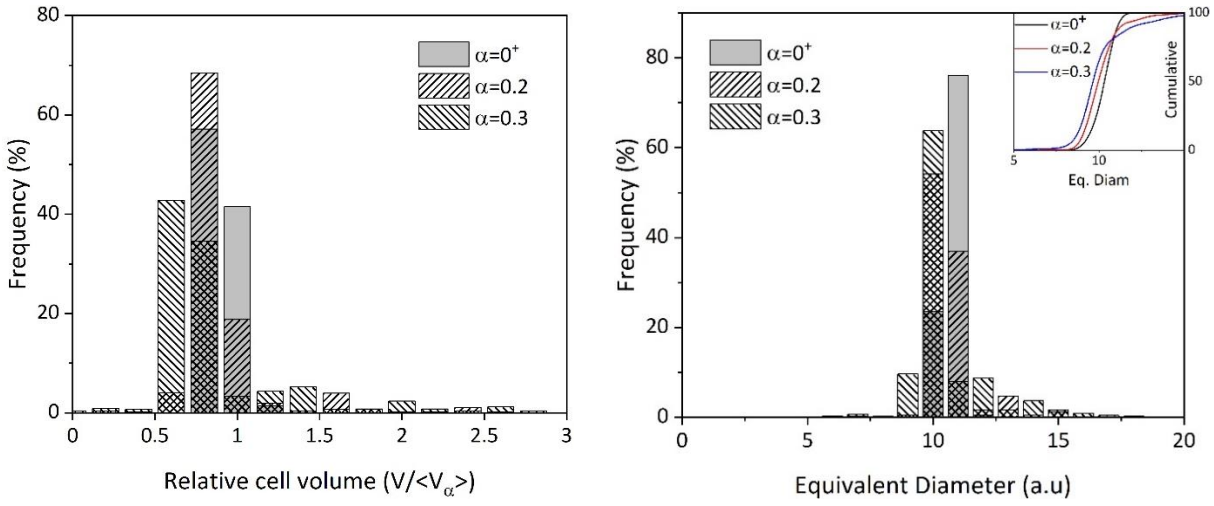

Fig. 5. (Left) Normalized cell volume distribution for different randomness levels and (Right) the corresponding equivalent cell diameters distribution

The polydispersity of the foam structure increases with disturbance of the cell seeds, witnesses by a broadening of the cell volume distribution despite a fairly constant average cell volume. It is worth noting that individual cell volumes can reach up to three times the average cell volume for the highest α value. The same trends can be observed in the distribution of the equivalent diameters (Fig. 5).

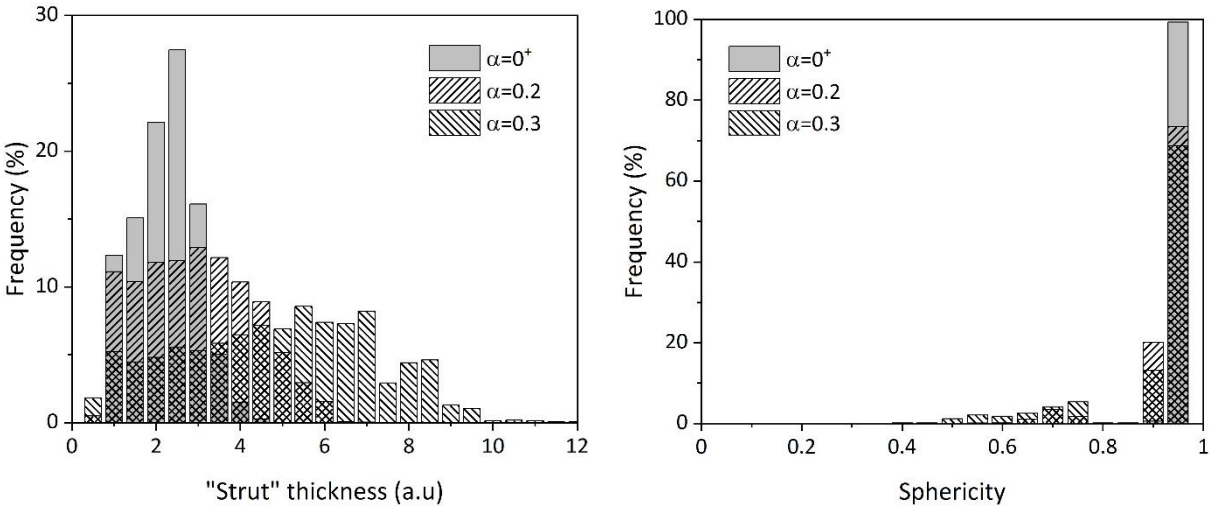

Fig. 6. Distribution of the cell wall thickness (Left) and of the sphericity (Right).

When $\alpha = 0^+$ one main central position appears on the histogram of the equivalent diameter distribution. However, for $\alpha > 0.1$, two or three different equivalent diameter groups characterize the overall microstructure. The rather reduced sphericity values are consistent with the idea of irregular cell shapes of this anisotropic microstructure (Fig. 6). Increasing α decreases the average cell sphericity by producing more distorted cells in the final structure. Indeed, Fig. 6 shows that the sphericity distribution is widen as α increases.

The walls of the cells along with the cell size have an impact on the mechanical properties of the foams: the variations in the wall thickness or in their geometry affect the apparition of mechanical instabilities, such as buckling, in accordance with the second moment of area. Figure 6 presents the strut thickness according to the magnitude of the perturbation. For a microstructure close to monodisperse ($\alpha = 0^+$), one logically remarks that the range of the cell wall thickness values is narrowed around an average value of 2.2 ± 1.1 (a.u). When α increases, the cell wall thickness distributions widens while its average values increase. This observation agrees with the previous analysis of the cell size distributions that indicate an increased number of large and small cells with the distortion. It is worth mentioning that the differences in wall thicknesses can result in the occurrence of an earlier onset cell collapse, that is suggesting different mechanical behavior.

The mean characteristics of the numerical samples are summarized in Table 1. The values reported for the porosity are the ones directly calculated from the meshed volumes used for the subsequent finite element calculations. The C_{vol} parameter used to quantify the dispersion of the cell size shows the same trend. In the case of "regularly" spaced cells, with $C_{vol} = 0.07$, the cell size distribution is rather narrow while it becomes wider for α = 0.3, for which C_{vol} reaches a value of 0.59.

α	**0^+**	**0.2**	**0.3**
Porosity	0.620	0.616	0.618
$<D_{eq}>$	11.2±0.27	11.14±0.86	11.04±1.65
$<C_{vol}>$	0.07	0.28	0.59
$<S_{ph}>$	0.97	0.94	0.91
$<C_{sph}>$	$8.7.10^{-3}$	$6.4.10^{-2}$	$1.2.10^{-1}$

Table 1. Mean geometrical parameters for the numerical foam samples

The structure of the foam is also revealed through the positions of the cells and the neighborhood relations between the bubbles. The average contact number $<Z>$ has been shown to be an important parameter to rationalise foam mechanics: $<Z>$ increases with porosity [58-61] and the structure becomes more rigid with increasing $<Z>$ [65-66]. Furthermore, the cell positions and contact number are an experimentally accessible quantity, which can help to relate the structure of the real foams to our simulated models. However, due to the deformability of the bubbles, a clear definition of a contact between two neighboring cells cannot rely on the

distance between their centroids, as this does not accurately predict the distance between their interfaces. We thus propose a new distance metric based on the surface-to-surface (S2S) method and a numerical implementation allowing for its computation on the minute timescale.

To determine the contacts, a test set of contact pairs is determined by applying a Delaunay triangulation to their centroid position. The S2S distance is then computed for each pair to determine the existence of a "contact". For every test pair, the voxels used to compute the pair distances are selected as being inside a cylinder joining the two centroids, as represented in Fig. 3 (left). We compute all the distances between pairs of voxels from different cells, as shown in Fig. 3 (right). This part is computationally expansive, and thus performed using a C algorithm. All the pair distances are then stored in a file associated to the pair of cells. In the last step, we summarize this file by associating each cells pair to the 5^{th} centile of its pair distance distribution represented in Fig. 3, taken as the S2S distance between the two cells. The final list of pairs associates every test pair with a S2S distance. A selection by the user of a threshold distance can further discriminate between "touching" and "non-touching" cell, depending on the physical properties of the considered foam.

The average contact number $<Z>$ is shown in Fig. 7 as a function of the distance threshold d_{thresh}. For the foam with a minimal disorder in its initial structure ($\alpha = 0^+$), $<Z>$ quickly reaches a plateau at $< Z > = 13.38 \pm 0.71$. This value is close to the values expected for ordered foams (it would be 14 for BCC and 13.5 for Weaire-Phelan [67]) and for disordered foams (13.7) [68]. For Laguerre tessellations – which approximate fairly well foam microstructures - the range is between 13 and 15.5 [69]. This value is, however, higher than expected for an FCC structure. Therefore, the average contact number was computed for a regular FCC lattice of perfect spheres for comparison. In that idealized case, the number of neighbors first increases to 4, corresponding to the neighbors distant from one basis vector, before reaching a plateau around 12. The variations in the number of neighbors come from the discrete representation of the interface on a square grid. Hence, the number of neighbors for the numerically generated foams is higher than that of an FCC foam: this difference may come from the generation procedure, and in particular the elastic and viscous stresses in the continuous phase during the cell growth giving polygonal curved shapes [24]. The beginning of this plateau is defined as the distance threshold for the other foams.

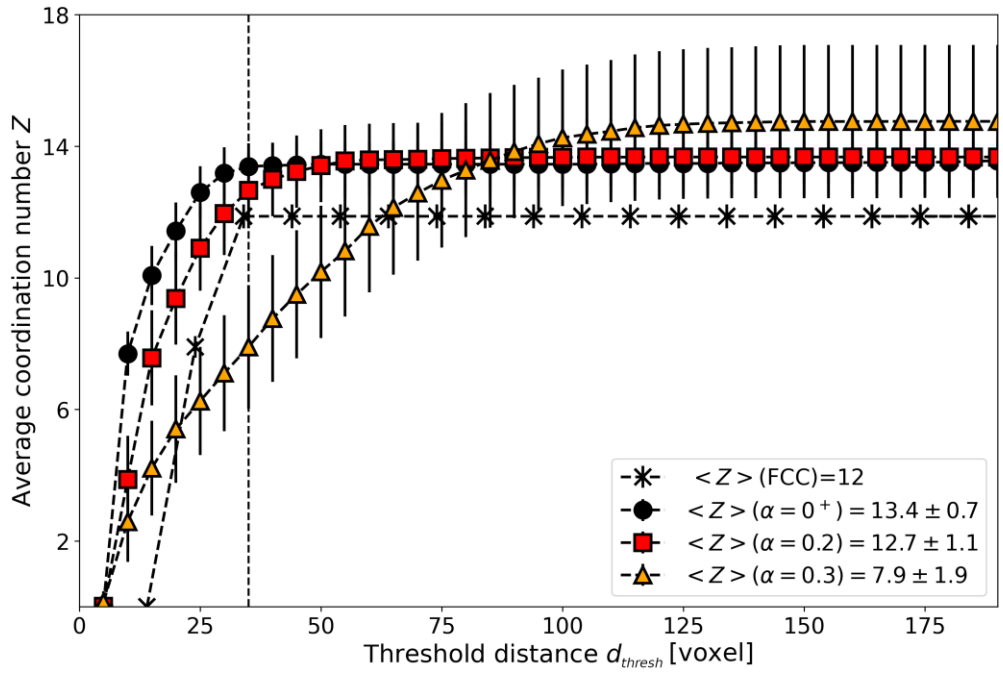

Fig. 7. Evolution of the average "contact" number < Z > with the threshold distance d for contact definition. D_{thresh} is chosen as the position of the plateau in <Z> for the foam with minimal disorder in initial structure ($\alpha \approx 0$).

The local geometrical organization is probed with the bond orientational order parameters [70, 71]. These are of course not mean chemical bonds, but rather distance-line resulting from some convenient assignation of near neighbors. The distance threshold for neighbor determination is taken from the contact number determination, shown in Fig. 7. The (q_4, q_6) coordinates of each cell is represented in Fig. 8, as well as their averaged coordinates. The q_6 parameter decreases with the disturbance parameter α, while the q_4 increases, indicating a change in the structural order from the initially FCC structure to an increasingly disordered state, different from the values obtained for regular lattices.

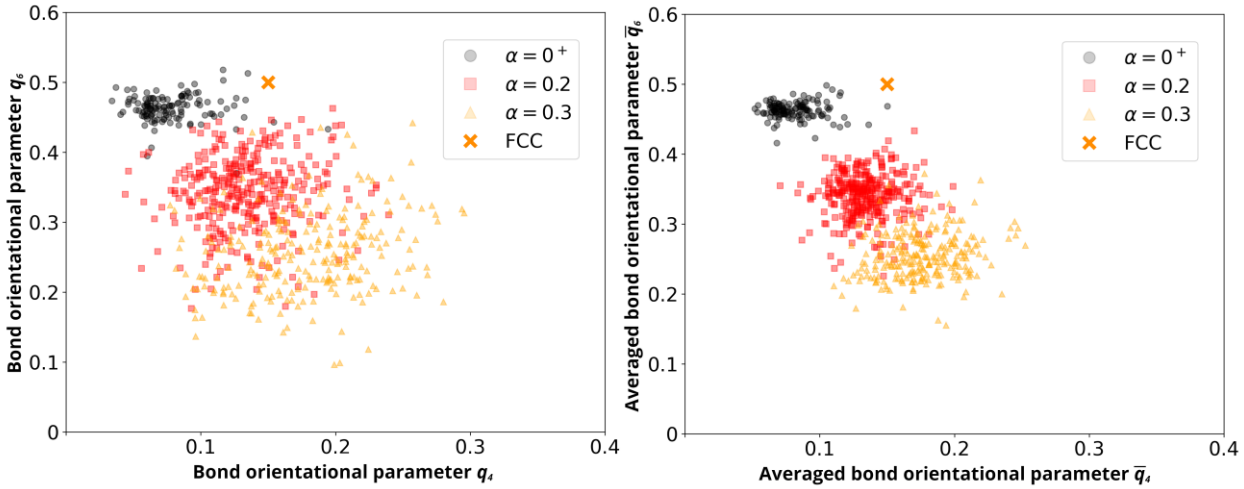

Fig. 8. Bond orientational order parameters (q4, q6) as well as their averages for the three different foams of Fig. 2. The contacts are determined using S2S distances and the plateau distance of <Z> as a threshold. The values for every cell are computed using the Pyboo library [50]. Values for FCC are taken from [71].

The large-scale structure of the foams is also investigated using the radial distribution function $g_2(r)$ and the Shannon entropy $H(n)$ [72, 73, 51]. The radial distribution function is computed using the centroid positions as interparticle distance r, as the computational cost of calculating S2S distances for all pairs of particles slows down the analysis to a major extent. The results are shown in Fig. 9. The most organized foam structure shows strong peaks corresponding to an FCC structure. For an increasing α, the peaks reduce in height and broaden in width, indicating a less localized distribution of neighbors in the first shells. For instance, the second peak splitting disappears for $\alpha > 0.2$, and the correlation disappears beyond the first peak for strongly randomized foam structure $\alpha = 3$. In the same vein of the bond orientational order parameters evolution of Fig. 8, this loss of correlation indicates the vanishing of long-range order in the foam with increasing randomness in the positions of the nucleation sites.

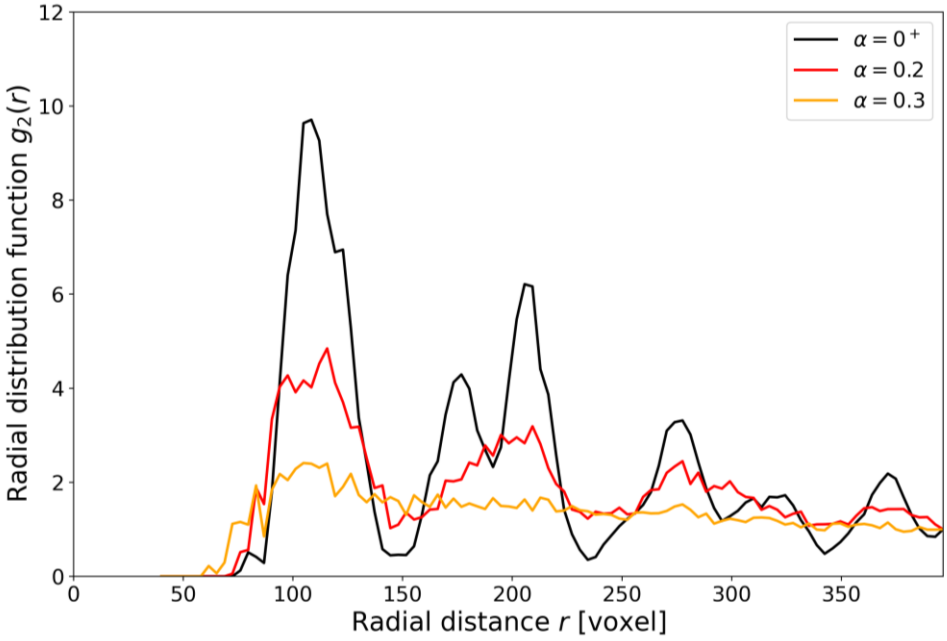

Fig. 9. Radial distribution function for the three different foams. The positions of the centroids are used to compute the distances.

The Shannon entropies of the three foams are computed following the procedure described in [73]. The contacts between the cells used for the determination of the contact network are defined in the same manner as for the average contact number and the bond orientational order parameters. The resulting Shannon entropy H as a function of the cluster size n is shown in Fig. 10. The average entropy increases with the structure randomization factor, going from $\sim 1.2\ k_B$ for the most regular lattice ($\alpha = 0^+$) to $\sim 1.4\ k_B$ for the most disorganized one ($\alpha = 0.3$).

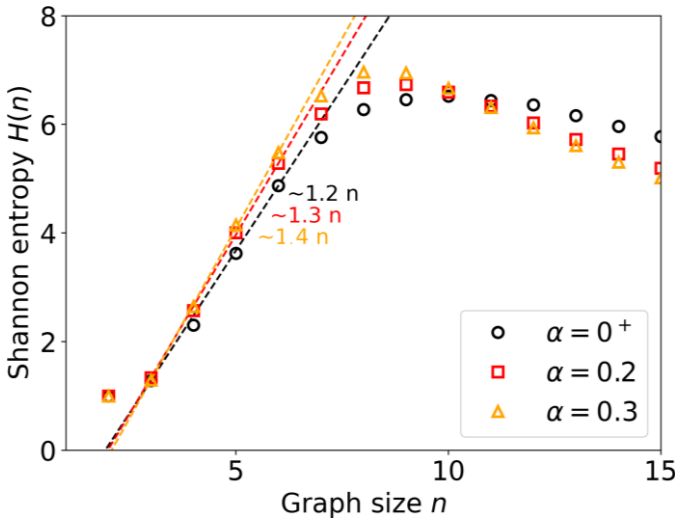

Fig. 10. Shannon entropy for the three numerical foams. The slope of the linear fit between n=2 and n=5 gives the average entropy per cell, expressed in units of the Boltzmann constant k_B.

Our characterization of the numerical foams found structural features that evolve with the degree of randomness in the nucleation structure. The initial structure is close to a face-centered cubic structure, as intended. Interestingly, the average contact number $<Z>$ is found to be closer to the one expected for foams ($<Z> \approx 13.7$) than the one for FCC structures ($<Z> = 12$), potentially indicating a strong physical relevance of our neighbor determination method. Also, it reveals the good representativeness of the numerically generated foam structures. Similarly, the bond orientational order parameters (q_4, q_6) evolve with the structure randomness, with broader distributions and values differing from the FCC results. These observations correlate with the disappearance of long-range correlation observed in the pair correlation function $g_2(r)$, even for a computation based on the centroid position. Finally, the increase of Shannon entropy per cell strongly correlates with the structure randomness and is thus a good candidate to evaluate the randomness of a bulk structure based on the physical contacts between the cells.

III.2. Mechanical Properties

The computed compressive stress–strain curves for the foam of different regularity are plotted on Fig. 11. The profiles reproduce the typical behavior of a cellular material, notably: a linear regime, a stress plateau, also called the plateau regime until the onset of the densification marked by an increase in stress. However, for closed-cell polymer foams and because of a relatively high density, the stress plateau regime shows a gradual stiffening of the response resulting in a steep slope, as opposed to low-density open cell polymeric foam which exhibit a neat plateau with a close to zero slope. The entrapped gas in the cells and the inner cell contacts are the reasons for the weakly marked transition between the linear response and the plateau stress. The onset of the densification step was identified by locating inflection points using the second derivative. At this stage, the cell walls crush together and come into contact so that the stress increases.

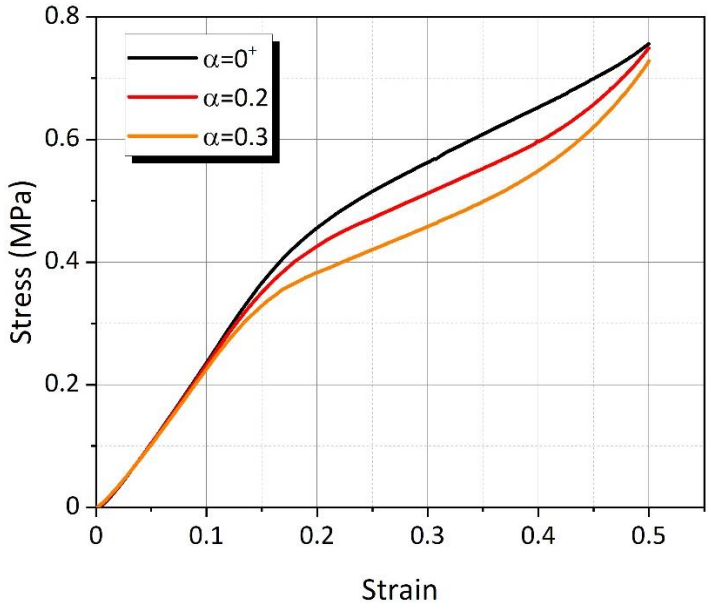

Fig.11. Compressive stress-strain curves obtained for foam with varying regularity.

III.2.1. Influence of perturbation degree on the elastic domain

A rich body of literature on foam mechanics has sought to establish an analytical expression between stiffness, the properties of the constituent material, and foam morphology, with Young's modulus being by far the most extensively studied mechanical characteristic. Table 2 lists the different formulae with the corresponding Young's modulus values. Note that the Voigt equation [74] is the upper bound which represents the best achievable stiffness for a cellular solid.

	Ref.	***E_f (MPa)***		***Refs.***	***E_f (MPa)***
$\frac{E_f}{E_s}=\frac{\rho_f}{\rho_s}$	[74]	3.82	$\frac{E_f}{E_s}=C_1\phi^2\left(\frac{\rho_f}{\rho_s}\right)^2+C_2(1-\phi)\left(\frac{\rho_f}{\rho_s}\right)$	[4] [1]	1.65 1.84
$\frac{E_f}{E_s}=\frac{1}{6}\left(\frac{\rho_f}{\rho_s}\right)$	[86]	0.64	$\frac{E_f}{E_s}=\frac{\rho_f/\rho_s}{1+C_{HS}(1-\rho_f/\rho_s)}$	[81]	2.36
$\frac{E_f}{E_s}=C_1'\left(\frac{\rho_f}{\rho_s}\right)^n$	[22] [87]	1.79 1.30	$\frac{E_f}{E_s}=\frac{2(7-5\nu_s)}{3(1-\nu_s)(9+5\nu_s)}\left(\frac{\rho_f}{\rho_s}\right)$	[82]	1.92

Table 2. Analytical estimate of foam relative Young's modulus according to different authors, where E_f and E_s designate the Young's modulus of foam and cell wall material respectively, ρ_f the density of the foam and ρ_s the bulk density. In these expressions, C_1, C_1', C_2 and n are constants; ϕ is the solid fraction in the cell edges; C_{HS} depends on the bulk Poisson's ratio ν_s (C_{HS}=0.98 for ν_s=0.4).

The results in Fig.11 suggest that the elastic domain is relatively insensitive to the microstructural arrangement of cells, as displayed by the superposition of all the curves. A Young's modulus of 2.3 MPa is obtained and can be compared with the values in Table 2. Strictly speaking, the Young's modulus for the regular structure ($\alpha = 0^+$) is a bit higher than for

the randomized one (α = 0.3) closer to 2.25 MPa. The same trend was observed by Sotomayor [75] and Duan [76] although with higher proportions. It should be mentioned that the opposite trend is obtained when periodic boundary conditions are used [38, 77]. To explain this finding, one can discuss the first equation of the second column in Table 2, which is the most used equation. Although unrealistic cubic cells were used, the ingenuity of Gibson and Ashby theory [1] was to combine in the same equation a first-degree term which reflects cell-wall stretching and a quadratic term which reflects cell-wall bending, thus taking into account the major mode of deformation observed in closed-cell foams. Low-density foams present microstructures that closely follow the basic rules set by the geometric stability as given by J. Plateau (1873) [13]. As such, four materials members (struts) meet at tetrahedral angles which cause the structure to be compliant or floppy in respect to a resulting negative Maxwell's criterion. This reveals why very low-density foams are almost always bending-dominated. For this reason, it is likely that good agreement between experimental data and the Gibson-Ashby's equation is usually found when $0.6 \leq \phi \leq 0.8$. However, real cellular materials exhibit much more complex microstructures than cannot be captured by a simple unit-cell model and hence a larger dependence of E with ϕ does exist. Also, it has been proven that edge-bending and wall-stretching do not contribute linearly, rather both mechanisms are active simultaneously [22]. Thus, some fitting parameters are usually necessary for comparison with experimental data. In some cases, the properties predicted by "Gibson's equation" can be drastically different, especially when the cell faces are relatively thick or when members undergo torsional effects. To explain how the regularity can influence the elastic properties, an analytical expression was derived by X. Shi [78] using the spring-in-parallel model developed by H.X. Zhu [79]. Assuming that the cells in a Voronoï foam experience the same strain as N springs in parallel would do, the Young's modulus of the foam is:

$$E_f = \sum_{i=1}^{N} E_i P_v(E_i) \qquad Eq.\ (2)$$

where E_i is the Young's modulus of the ith cell and $Pv(E_i)$ corresponds to the volume probability of the cells with elastic modulus E_i. Also, the relative density of the foam is given by:

$$\rho_r = \frac{\rho_f}{\rho_s} = 1 - \sum_{i=1}^{N} \frac{V_i}{V} \qquad Eq.\ (3)$$

where V_i is the volume of the ith cell and V is the total volume. If P_i is the void volume proportion of the ith cell, and that $P_v(P_i)$ is the volume probability of cells having a porosity contribution of P_i then it comes:

$$\frac{E_f}{E_s} = C_1\phi\left(1-\sum_{i=1}^{N} P_i\right)^2 P_v(P_i) + C_2(1-\phi)\left(1-\sum_{i=1}^{N} P_i\right)P_v(P_i) \qquad Eq.\ (4)$$

in the framework of Gibson. This expression can be written as:

$$\frac{E_f}{E_s} = C_1\phi\left(1-\sum_{i=1}^{N} P_i\right)^2 P_v(P_i) + C_2(1-\phi)\rho_r \qquad Eq.\ (5)$$

Since this equation involves the volume probability of the porosities of the cells, and therefore their volume distribution, one can notice that only the term referring to the bending of the cell edges is sensitive to it. Thus, the regularity has an influence in foams with open cells, and for the lowest densities. Conversely, for closed-cell foams and especially for those having thick walls, cell-face stretching is predominant, and the structural regularity will not affect the elastic domain. Note that for a same porosity level, the cell volume distribution widens as irregularity increases, as shown in Fig. 5 and by the $g_2(r)$ function in Fig. 9. Also, for open-cell foams, the trend would be that irregularity inducing a higher volume fraction of large volume cells leads to a reduced modulus of elasticity [80].

The ϕ parameter refers to the amount of matter in the cells edges (struts) and therefore the lower it is, the more the first order term of the equation will drive the response. Note that considering most of the solid fraction in the cell face, the solution given by Gibson-Ashby equals the Voigt bound and overestimates the modulus value. In this case, the foam relative Young's modulus is best approximated by the theory for composites using different homogenization methods. This explains why the Hashin-Shtrikman's (HS) solution [81] is quite close to our present result. Christensen's [82] solution is also acceptable. These two solutions are derived from the theory of composites: for one (HS), it is based on the theory of elasticity by Eshelby [83] and for the other, it is obtained by applying the mean field theory to a composite made of randomly located spherical inclusions. In both cases, the voids are considered using inclusions having vanishing properties. Interestingly, even if Hashin-Shtrikman's solution refers to Eshelby theory assuming dilute volume fraction which implies uniform stress and strain fields, it has been proven that satisfactory results are obtained for moderate to high void volume fractions. In particular, numerical investigations and experiments on closed-cell foam revealed that bulk and shear moduli lie very close to the theoretical Hashin-Shtrikman upper bounds up to porosities of 80% [84, 85]. First works proposed by Gent and Thomas [86] consider foam microstructures as networks of elastic threads subject to affine displacements at the joints. It is thus validated for a small volume fraction of solid material. From their side, Roberts and Garboczi [22] and more recently Redenbach [87] used F.E analysis of Voronoi or

Laguerre tessellations to derive scaling relationships between Young's modulus and density for closed-cell foams. However, the pre-factor being neither equal nor close to one, their analytical solutions are not suitable to high densities. To conclude on these aspects of regularity effect on elastic properties, Christensen [82] established the following in the case of very low density closed cell materials: the effective properties are independent of the exact geometry of the cell but only depend upon the volume fraction of the material. The present results seem to be generalizable to all porosities, in closed-cell case.

III.2.2. Influence of perturbation degree on the plastic domain

Fig. 11 shows an increase of the yield strength (σ_{pl}^{f}) as regularity increases: 0.28 MPa for α=3; 0.34 MPa for α=2 and 0.37 MPa for α=0^{+}. The same trend was observed by several authors who used Voronoi models to simulate closed-cell foams [77, 79, 88]. Intuitively, the regular arrangement creates cell walls of nearly equal cross-section which directly opposes the compression loading. As the irregularity increases, the cell walls become randomly oriented and have a wider thickness distribution which constitutes lower resistance intensities especially for the inclined struts of low cross-sectional area. These thin areas tend to collapse first under the effect of the load. A transition from a diffuse deformation throughout the foam to first strain localizations occurs. This results in the appearance of highly bent faces among the cells of the foam. As bending events occur in "cascade", the compression curve exhibits an inflection or curvature which intensifies as the strain increases, as shown in Fig. 11 for α=0.3 and 0.2. For the regular structure, the mechanism of deformation is quite different. A transverse shear band to the loading appears progressively and propagates throughout the foam as strain increases. Then the post-yield stress increases with different slopes depending on the degree of perturbation. The compression of the gas within the cells, together with the membrane stresses which appear in the cell faces, are the reason for this rising part of the curves. It is however not straightforward to distinguish the contribution of each one.

Gibson and Ashby [1] predicted the plastic collapse of foams $\left(\sigma_{pl}^{f}\right)$ through equation (6). This equation combines the effect of plastic bending of cell edges and plastic stretching of their faces. The gas effect being driven by the difference P_0-P_{at}, when the initial gas pressure in the cells equals the atmosphere pressure, no influence on the value of the elastic limit can show up:

$$\frac{\sigma_{pl}^{f}}{\sigma_{ys}} = 0.3\left(\phi\frac{\rho_f}{\rho_s}\right)^{3/2} + 0.4(1-\phi)\frac{\rho_f}{\rho_s} \qquad Eq.\ (6)$$

where σ_{ys} is the yield strength of the bulk constitutive material.

In a similar way, Simone and Gibson [4] found an approximation for the ratio given by:

$$\frac{\sigma_{pl}^{f}}{\sigma_{ys}} = 0.44\left(\frac{\rho_f}{\rho_s}\right) + 0.32\left(\frac{\rho_f}{\rho_s}\right)^2 \qquad Eq.\ (7)$$

While the surrogate model developed by Marvi-Mashhadi *et al.* [89] predicts:

$$\frac{\sigma_{pl}^{f}}{\sigma_{ys}} = 0.156\phi^{3.5}\left(\frac{\rho_f}{\rho_s}\right)^{3/2} + 0.76(1-\phi)\left(\frac{\rho_f}{\rho_s}\right)^{3/2} \qquad Eq.\ (8)$$

The predictions of the plastic collapse of foams by equations (6), (7) and (8) are compared with the result of our developed numerical simulation in table 3. The fraction of solid in the strut was calculated from the analysis of the digital foam microstructures using a dedicated tomography software: VG Studio. A ϕ value of 0.2 was found. This is consistent with the type of the present studied foams. Note that at the limiting case and because of relatively high density (ρ_r=0.38), several authors have considered only cells face, i.e. ϕ=0 [1], an assumption that cancels the first terms in Eqs. (6) and (8). A good agreement is found between the models and the present simulation results. It is worth noting that equations (6)-(7) were determined using a tetrakaidecahedron cell, however, for equation (7), uniformly thick cell faces were assumed (i.e., with no plateau border). As the transfer of material from the struts to the cell walls increases the plastic-collapse stress with respect to higher in-plane axial deformation, it is not surprising that the highest value is obtained with such a model.

Eq. (6)	Eq. (7)	Eq. (8)	Present work
0.25 MPa	0.42 MPa	0.28 MPa	0.28-0.37 MPa

Table 3. σ_{pl}^{f} for closed-cell foam according to eq. 6-8 and values obtained by the present study. For the calculation: relative density, ρ_r=0.38 and ϕ=0.2.

The similarity of the results given in Table 3 suggests that the analytical models involve the relevant deformation mechanisms, the same ones that are involved in the FE simulation. Plastic collapse causes the cell walls to crumple in the compression direction, while the faces stretch increasing the contribution to the strength. This is assessed by calculating the fraction of the material that is contained in the cell faces, as discussed previously. These observations go concomitantly with the previous calculation of the Young's modulus, which reflects an important contribution from the cell walls.

The effect of the gas pressure actually depends on the reduction of the foam's volume during compression, which in turns depends on the Poisson's ratio of the foam v_f. If the foam is

compressed axially by a strain ε, then the volume reduction is given by the volumetric strain: $\varepsilon_v = \varepsilon(1-2\upsilon_f)$ and part of gas pressure creating an overpressure:

$$\Delta p = \frac{P_0\varepsilon\left(1-2\upsilon_f\right)}{1-\varepsilon\left(1-2\nu_f\right)-\rho_f/\rho_s} \qquad Eq.\ (9)$$

Taking the limit at small strain of the derivative, the gas contribution to the foam stiffness is:

$$E_{gas}^{f} = \frac{P_0(1-2\nu_f)}{1-\rho_f/\rho_s} \qquad Eq.\ (10)$$

The Poisson's ratio of the numerical foams was determined using the nodal lateral strain in the two directions perpendicular to the loading direction divided by the applied strain. A value in the range [0.31 (α=0.3), 0.34 (α=0.2), 0.37 (α=0^+)] was obtained which is consistent with the model of Christensen which gives 0.35 [82]. Gibson and Asbhy [1] assume a Poisson's ratio of 1/3 regardless of the foam density. The decrease of Poisson's ratio with the disturbances is in agreement with the observations given by Barbier *et al.* [77] for 3D Voronoi structures. Considering P_0 is atmospheric pressure, gas contribution to the stiffness is only 0.04 MPa which represents less than 2% of the Young's modulus. On the other hand, the relatively high value of the Poisson's ratio induces a low reduction of the foam volume during compression, thus a small increase of the gas pressure within the cells.

One way to identify the contribution of the gas in the post-collapse plastic regime is to model the stress evolution writing:

$$\sigma_{post}^{f} = \sigma_{pl}^{f} + \frac{P_0\varepsilon}{1-\varepsilon-\rho_f/\rho_s} \qquad Eq.\ (11)$$

where σ_{pl}^{f} refers to the elastic limit of the foam.

Then, if the gas effect is the main contribution to the stress rising, the post-collapse stress should vary linearly with $\frac{\varepsilon}{1-\varepsilon-\rho_f/\rho_s}$ with a slope corresponding to P_0. Figure 12 shows such a plot for the different numerical foam microstructures. One can notice that the stress approximation by eq. (11) assumes a Poisson's ratio of the foam being zero. By taking values close to 0.3, the effect of the gas is much more reduced as volumetric strain decreases when ν_f increases. The results (Fig. 12) demonstrate that the complete behavior cannot be described by eq. (11), however it allows some phenomenological interpretation. In the very beginning of the post-collapse domain, the curves are non-linear, then the linear fitting parts show slopes that differ from P_0 by about a factor of two. Also, the intercepts do not correspond to the elastic limits of the foams. We conclude that compression of the cell gas does not contribute much on the rising of the post-collapse stress. Here, because of the relatively high density, thick cell walls carry

most of the load above the level needed just to compress the gas. The plastic collapse is mainly affected by the bending and the stretching of the cell walls. As the edges and the cell walls bend, in the perpendicular direction to the loading, thick cell walls are stretched and because of their relatively high stiffness, a steady step rising of the plastic stress is observed. It follows that the non-linear behavior observed for the post-collapse stress comes from maximum stress localization and encompasses the non-linear strain hardening behavior of the constitutive material. It is worth noting that under the same level of stress, the disordered cellular structure is more severely deformed than the regular one. Therefore, the gas pressure inside the cells acts differently depending on the cell arrangement (topology). This can be observed from Fig. 12 that shows an increasing gas contribution through a steeper slope, as α increases. Also, the intercept is lower compared to the case $\alpha=0^+$ which indicates a reduced contribution from the constitutive material. To better interpret the gas behavior, one can compare the carrying capacity provided by the gas overpressure between an FE foam model including the gas behavior and one not including it. All the other simulation parameters being the same, the results are shown in Fig. 13. The irregularity may create weak cross-sections with small areas and greater misalignments with respect to the loading direction which inevitably lead to strain localization. The deformation mechanisms of the different foams are depicted in Fig. 14 as a function of the applied compressive strain. For random structures, a cell layer collapses in a row forming a localized shear band while the deformations are preferentially confined to cell walls parallel to the loading for regular structures (Fig. 14).

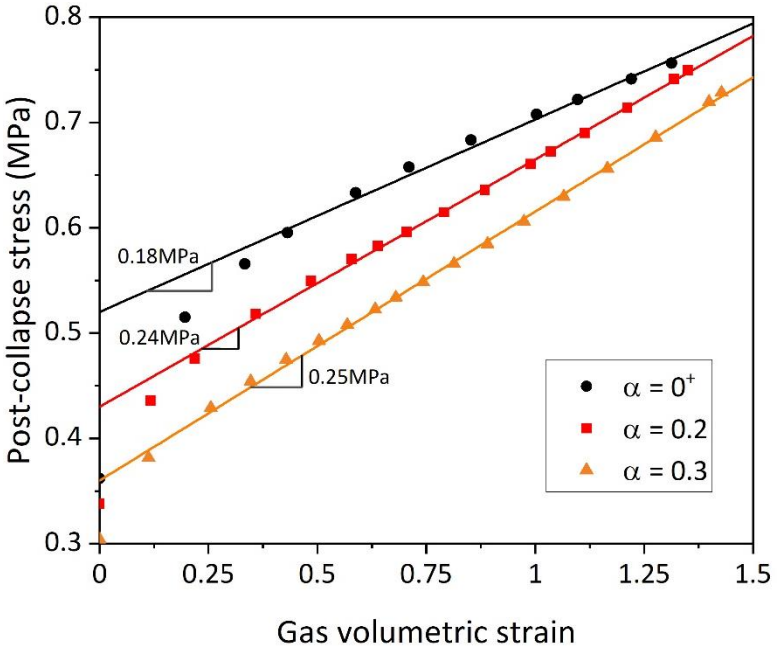

Fig.12. Post-collapse stress σ_{pl}^{f} against gas volumetric strain for the studied foam structures. The solid lines represent the linear fitting curves given by eq (11).

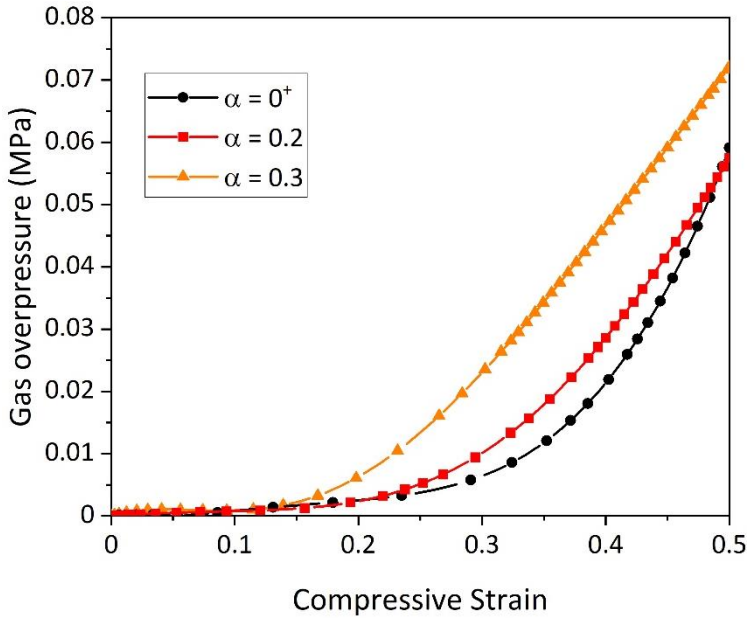

Fig. 13. Contribution of the gas pressure inside the cells for α=0⁺, α=0.2 and α=0.3 obtained by comparison of FE calculations between ad-hoc foam models including the gas effect or not.

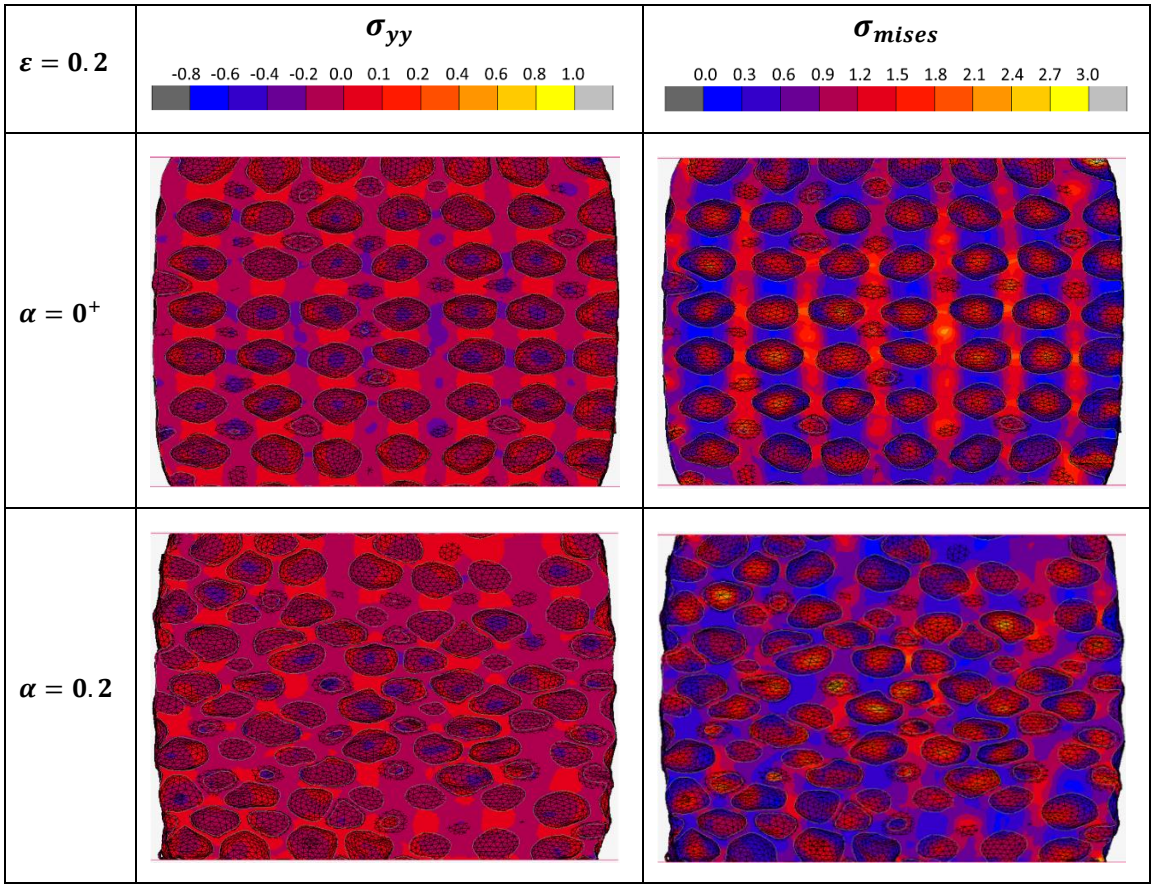

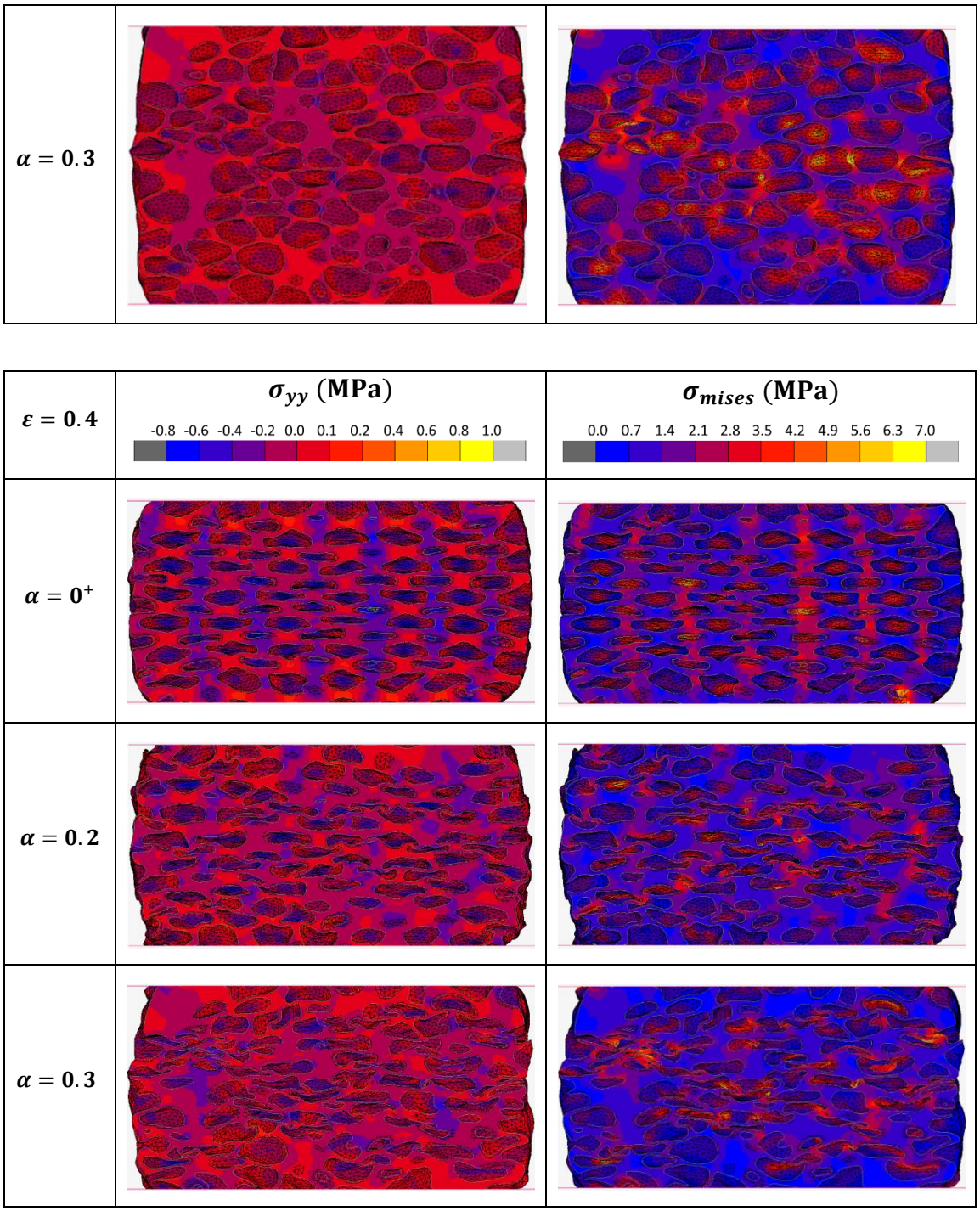

Fig. 14. Contour plots of the normal compressive and the Von mises stresses for regular ($\alpha=0^+$) and irregular foam microstructures ($\alpha=0.2$; $\alpha=0.3$) when compression is applied from the top and at a strain level of $\varepsilon=0.2$ and $\varepsilon=0.4$.

To summarize the post-collapse behavior, the regular organization efficiently opposes compressive stress and appears more resistant because most cell walls are nearly perpendicular to the loading direction. In the mechanical response, a weaker role of the gas is thus observed

when $\alpha=0^+$ as indicated by the lower slope value compared to the others, while the intercept is superior to any others (Fig. 12). The irregularity causes an earlier contribution of the gas, from the first stages of compression as shown in Fig. 13. We can identify the first rises in pressure from the beginning of the plateau domain for α=0.2 and α=0.3. In this case, the buckling of the cell walls lead to high local strain which triggers the gas compression. Thus, the behavior of the gas and that of the constitutive material interact in different proportions during compression. Depending on whether the structure is ordered or random, the proportion of one relative to the other varies. As a result, the plateau stresses increase more or less rapidly until the final stage of densification. The same applies to the onset of densification. Disordered structures tend to collapse more rapidly, causing cell walls to crush together more easily and leading to earlier densification. At this stage, some cell walls come into contact, and the resulting contact forces amplify the gas compression effect. Thus, as densification progresses, even as gas pressures in the cells converge across different models, the contribution of contact forces becomes more significant in heterogeneous models. This aligns with the observed strain hardening at large deformations. For further description, due to the restricted strain range of the present study, less than 50%, the pressure effect in the cell remains limited. The limiting strain ε_D for the onset of densification can be assessed using the empirical expression [1]: $\varepsilon_D = 1 - 1.4\rho_r \cong 0.46$. This confirms a strain limit near the beginning of densification, in agreement with the shapes of the stress-strain curves (Fig. 11). However, gas pressure effects may become more pronounced at larger strains, particularly when the constituent material is soft and considering the absence of gas diffusion.

Within the porosity range selected for this study, the local stress field induced by compression results from a combination of compressive/tensile loading, as well as bending and even localized shear, which gradually lead to structural collapse. At the structural scale, wall thickness data alone are insufficient to predict enhanced mechanical resistance. Indeed, Figure 14 shows that the ordered structure is subjected to a tensile/compressive stress field aligned with the principal directions of the cell walls. The change in behavior induced by structural disorder is strongly influenced by the degree of strut inclination.

From a mechanical standpoint, the polar representation of a beam's second moment of area is sufficient to demonstrate that it can drop rapidly along certain orientations (typically near 45°), thereby diminishing the effect of beam thickness. It is thus essential to characterize the microstructure in terms of its 'tortuosity' as well. Referring to the work of Lanfrey et al., the tortuosity of a random particle assembly is inversely proportional to the square of its sphericity. An increase in the parameter α not only shifts cell orientation, as evidenced by the change in

sphericity (Fig. 6), but also broadens the thickness distribution. For the thinnest stuts, misalignment (relative to the loading direction) exacerbates the loss of mechanical strength. Figure 14 highlights these mechanisms by revealing a growing heterogeneity in stress fields as compression intensifies.

IV. Conclusions and outlook

To understand the mechanical behavior of solid foams, the influence of cell distribution is often sought. As such, many studies on the topic can be found in the literature. However, most of them relate to open-cell foams of very low density and for which the cellular structures are schematized by geometries meeting surface minimization criteria. In the present study, we have focused on the mechanics of closed cell foams of medium porosity by endeavoring to represent the cellular structure as realistically as possible. To achieve this goal, an *ad-hoc* modeling method following our on-going work presented in a previous publication was used as it demonstrated being capable of simulating industrial foam structures with great realism. Three types of foam structures were generated, differing by the degree of order in the arrangement of their cells. It is worth noting that the numerical microstructures being representative of commercial foams, the regular system does not mean perfectly aligned spheres as could be obtained with CAD software. The numerical foams showed an average number of neighbouring cells close to that expected for real foam which is about 13.7. Also, pair correlation function indicates a clear vanishing of long-range order with increasing randomness of the cell arrangement in foams. As a consequence, the distribution of the cell walls thicknesses is broadened as randomness increases. The same applies to cell volumes and their anisotropy with an increase in polydispersity and sphericity when the cell organization is increasingly random. The mechanical behavior in compression of the closed-cell foams was simulated up to 50% (revealed as being the onset of densification) by means of finite element analysis. The simulations include the influence of the gas pressure in the cells and that of the contact when opposing cell walls crush against each other. The Young's modulus was revealed as insensitive to the cellular microstructure and its variations. For large compressive strain, the plastic collapse strength decreases when the cellular structure becomes disordered. However, the stress increases continuously with strain for all the structures, but the causes are not exactly the same. In the first stage of deformation, the regular foam is compressed uniformly and is prone to develop cell walls stretching which prevent gas compression. Thus, the mechanical response is first driven by the cell walls stresses reflecting part of the constituent material behavior. After

this first step of wall stretching, the stress-strain curve then rises as the cells are squeezed creating gas overpressure. In irregular foams, the distribution of cell volumes is broader, leading to greater variations in wall thickness. As a result, those of smallest areas or inclined with respect to the loading direction first collapse. Next, plastic buckling appears successively and forms a transverse band that propagates throughout the foam. Thus, the irregular foam deforms more than the regular one for a same level of the applied stress and the effect brought by inner cells gas compression is revealed earlier. There follows a gradual stiffening proportional to the combined effects of the strain hardening of the constituent material, of the gas overpressure and of the inner contacts. For both types of foam, whether organized or not, the response after the initial elastic domain is one of monotonic increase with no distinct plateau stress or densification region. It is however verified that regularity results in stiffer response with a higher plateau stress.

CRediT authorship contribution statement

T. Roland: Writing – original draft, Visualization, Validation, Software, Methodology, Formal analysis, Supervision. G. Ginot: Writing – review & editing, Methodology, Investigation, Data curation. M. Dabo: Investigation, Software, Methodology, Conceptualization. C. Gauthier: Writing – review & editing, Investigation, Supervision. W. Drenckhan: Writing – review & editing, Investigation, Supervision. P. Kékicheff: Writing – review & editing, Formal analysis, Investigation.

Declaration of competing interest:

The authors declare that they have no known competing financial interests or personal relationships that could have appeared to influence the work reported in this paper.

References

[1] L. J. Gibson, M. F. Ashby (1997), *Cellular solids: Structure and Properties*, 2nd ed., United Kingdom: Cambridge University Press, Cambridge

[2] E. Pardieu, N.T.T. Chau, T. Dintzer, T. Romero, D. Favier, T. Roland et al., Polydopamine-coated open cell polyurethane foams as an inexpensive, flexible yet robust catalyst support: a proof of concept. *Chemical Communications*, 2016, *52*(25), 4691–4693.

[3] JD. Bobyn, RM. Pilliar, HU. Cameron, GC. Weatherly, The optimum pore size for the fixation of porous-surfaced metal implants by the ingrowth of bone. *Clinical Orthopaedics and Related Research*, 1980, 150, 263-270.

[4] A. Simone, L. Gibson, Effects of solid distribution on the stiffness and strength of metallic foams. *Acta Mater.* 1998, 46(6), 2139–2150.

[5] A. Simone, L. Gibson, The effects of cell face curvature and corrugations on the stiffness and strength of metallic foams, *Acta Mater.* 1998, 46(11), 3929–3935.

[6] A.M. Kraynik, M.K. Neilsen, D.A. Reinelt, W.E. Warren, *Foam micromechanics*. In: Proc. NATO Advanced Study, Institute on Foams, Emulsions and Cellular Materials (1998), Kluwer.

[7] A.M. Kraynik, W.E. Warren, The elastic behavior of low-density cellular plastics. In: Hilyard, N.C., Cunningham, A.C. (Eds.), Low Density Cellular Plastics. Chapman and Hall, London, (1994)

[8] W.E. Warren, A.M. Kraynik, Linear elastic behavior of a low-density Kelvin foam with open cells. ASME *J. Appl. Mech.* (1997) 64 787–793.

[9] W.-Y. Jang, A.M. Kraynik, S. Kyriakides, On the microstructure of open-cell foams and its effect on elastic properties. *Int. J. Solids Struct.* (2008) 45 1845–1875.

[10] L. Gong, W.-Y. Jang, S. Kyriakides, Compressive response of open-cell foams. Part I: morphology and elastic properties. *Int. J. Solids Struct.* (2005) 42 1355–1379.

[11] L. Gong, S. Kyriakides, N. Triantafyllidis, On the stability of Kelvin cell foams under compressive Loads. *J. Mech. Phys. Solids* (2005) 53 (4) 771–794.

[12] K.A. Brakke, The surface evolver. *Experimental Mathematics* (1992) 1 141–165.

[13] J.A.F. Plateau, Statique Expérimentale et Théorique des Liquides Soumis aux Seules Forces Moléculaires, vol. 2. Gauthier-Villars, Paris, 1873.

[14] H.X. Zhu, J.F. Knott, N.J. Mills, Analysis of the elastic properties of open-cell foams with tetrakaidecahedral cells. *J. Mech. Phys. Solids* (1997), 45, 319–343.

[15] J.L. Grenestedt, Influence of Wavy Imperfections in Cell Walls on Elastic Stiffness of Cellular Solids, *J. Mech. Phys. Solids* (1998), 46 (1), 29–50.

[16] J.L Grenestedt, K. Tanaka, Influence of cell shape variations on elastic stiffness of closed cell cellular solids. *Scr. Mater.* (1999), 40, 71–77.

[17] J.L. Grenestedt, F. Bassinet, Influence of cell wall thickness variations on elastic stiffness of closed cell cellular solids. *Int. J. Mech. Sci.* (2000) 42 1327–1338.

[18] W. Drenckhan, S. Hutzler, 2015. Structure and energy of liquid foams. *Adv. Colloid and Interface Sci*. (2015), 224, 1-16

[19] E. B. Matzke, The three-dimensional shape of bubbles in foam-an analysis of the role of surface forces in three-dimensional cell shape determination, *American Journal of Botany* (1946) 58-80.

[20] A.M. Kraynik, D.A. Reinelt, F. van Swol, Structure of random monodisperse foam, *Phys. Rev E Stat Nonlin Soft Matter Phys* (2003), 67, 031403.

[21] S.D. Papka, S. Kyriakides, In-plane compressive response and crushing of honeycomb. *J. Mech. Phys. Solids* (1994), 42, 1499-1532.

[22] A.P Roberts, E.J. Garboczi, Elastic moduli of model random three-dimensional closed cell cellular solids, *Acta Mater.* (2001), 49, 189–197.

[23] K. Li, X.L. Gao, G. Subhash, Effects of cell shape and strut cross-sectional area variations on the elastic properties of three-dimensional open-cell foams. *J. Mech. Phys. Solids* (2006), 54, 783–806.

[24] M. Dabo, T. Roland, G. Dalongeville, C. Gauthier, P. Kekicheff, Ad-hoc modeling of closed-cell foam microstructures for structure-properties relationships, *Eur. J. Mech. Solid* (2019), 75, 128-141.

[25] N. J. Mills, Deformation mechanisms and the yield surface of low-density closed-cell polymer foams, *J Mater Sci* (2010), 45, 5831–5843.

[26] TG. Zielinski, Generation of random microstructures and prediction of sound velocity and absorption for open foams with spherical pores, *J. Acoust. Soc. Am.* (2015), 137, 1790-1801.

[27] Z. Adamczyk, B. Siwek, M. Zembala, P. Weronski, Influence of polydispersity on random sequential adsorption of spherical particles. *J. Colloid Interface Sci.* (1997), 185, 236–244.

[28] M. Amon, C.D. Denson, A study of the dynamics of foam growth: Analysis of the growth of closely spaced spherical bubbles, *Polym. Eng. Sci.* (1984), 24, 1026–1034

[29] C.D Han. Multiphase Flow in Polymer Processing. *Academic Press*, 1981.

[30] W. Zhai, J. Yu, L. Wu, W. Ma, J. He, Heterogeneous nucleation uniformizing cell size distribution in microcellular nanocomposites foams, *Polymer* (2006) 47 7580–7589.

[31] L.W. Schwartz and R.V. Roy, A mathematical model for an expanding foam, *Journal of Colloid and Interface Science* 264 (2003) 237–249.

[32] Mixed Velocity-Displacement Formulation for Modeling of Complex Behavior of Polymer, Ph.D dissertation, Paris, ENMP, V.T. Pham, Coupez Thierry, Billon Noëlle.

[33] J.J. Feng, C.A. Bertelo, Prediction of bubble growth and size distribution in polymer foaming based on a new heterogeneous nucleation model, *J. Rheol.* (2004) 48 439.

[34] M.A. Shafi, J.G. Lee, R.W. Flumerfelt, Prediction of cellular structure in free expansion polymer foam processing, *Polym. Eng. Sci.* (1996) 36 1950–1959.

[35] M. Dabo, Analyse du comportement mécanique des mousses polymères : apport de la tomographie X et de la simulation numérique, Ph.D dissertation, CNRS/Université de Strasbourg (2015)

[36] S. Heitkam, W. Drenckhan, J. Fröhlich, Packing spheres tightly: influence of mechanical stability on close-packed sphere structures. Phys. Rev. Lett. 108, 148–302 (2012)

[37] H. X. Zhu, S. M. Thorpe, and a. H. Windle, "The effect of cell irregularity on the high strain compression of 2D Voronoi honeycombs," *Int. J. Solids Struct.*, vol. 43, no. 5, pp. 1061–1078, 2006.

[38] H. X. Zhu and A. H. Windle, Effects of cell irregularity on the high strain compression of open-cell foams, *Acta Materialia* (2002) 50 1041-1052.

[39] E.W. Andrews, G. Gioux, P. Onck, L.J. Gibson, Size effects in ductile cellular solids. Part II: experimental results. *Int J Mech Sci* (2001), 43 (3), 701–713.

[40] T. Kanit,S. Forest, I. Gaillet, V. Mounoury, D. Jeulin, Determination of the size of the representative volume element for random composites : statistical and numerical approach", international journal of solids and structures, (2003), 40(14) 3647-3679

[41] K. Li, X.L. Gao, J. Wang, Dynamic crushing behavior of honeycomb structures with irregular cell shapes and non-uniform cell wall thickness, *Int. J. Solids Struct.* (2007), 44, 5003–5026.

[42 K. Emori, T. Miura, H. Kishida, A. Yonezu, Creep deformation behavior of polymer materials with 3D random pore structure: Experimental investigation and FEM modeling, *Polymer Testing* (2019), 80, 106097.

[43] P. Srinivasa, A. Kulachenko, a three-dimensional numerical model for large strain compression of nanofibrillar cellulose foams, *Nordic Pulp and Paper Research Journal* (2018), 33(2), 256-270

[44] N. Gopala, K. Ehab, B. Sonon, T.J. Massart, L. Noels, Computational generation of open-foam representative volume elements with morphological control using distance fields, *European Journal of Mechanics A/Solids* (2019), 78, 103847.

[45] M. Yu, P. Zhu, Y. Ma, Effects of particles clustering on the tensile properties and failure mechanisms of hollow sphere filled syntactic foams: a numerical investigation by microstructure-based modeling, *Mater. Des.* (2013), 47, 80

[46] K Natesaiyer, C. Chan, S. Sinha-Ray et al, X-Ray CT imaging and finite element computations of the elastic properties of rigid organic foam compared to experimental measurements: insights into foam variability, *J. Mater. Sci.* (2015) 50 4012-4024.

[47] V.D. Nguyen, L. Noels, Computational homogenization of cellular materials, *International Journal of Solids and Structures* (2014) 51 11-12

[48] C. Miehe, A. Koch, Computational micro-to-macro transitions of discretized microstructures undergoing small strains, *Arch Appl Mech* (2002)72 300-317.

[49] github: https://github.com/SimianLibrarian/vritra

[50] M. Leocmach, Pyboo : a python package to compute bond orientational order parameters, 2017

[51] J. Brujic, C. Song, P. Wang, C. Briscoe, G. Marty, H. A. Makse, Measuring the coordination number and entropy of a 3D jammed emulsion packing by confocal microscopy, *Physical Review Letters* 2007, 98, 248001

[52] M. E. Evans, G. E. Schröder-Turk, A. M. Kraynik, A geometric exploration of stress in deformed liquid foams, *J. Phys.: Condens. Matter* (2017), 29, 124004

[53] R. Arevalo, I. Zuriguel, D. Maza, Topology of the force network in the jamming transition of an isotropically compressed granular packing, *Phys. Rev. E* (2010), 81, 041302

[54] M. Herrera, S. Mc Carthy, S. Slotterback, E. Cephas, W. Losert, M. Girvan, Path to fracture in granular flows : dynamics of contact networks, *Phys. Rev. E* (2011), 83, 061303

[55] R. Arevalo, I. Zuriguel, S. A. Trevijano, D. Maza, Third-order loops of contacts in a granular force network, *International Journal of Bifurcation and Chaos* (2010), 20(03), 897-903

[56] S. Blott, K. Pye, Particle shape: a review and new methods of characterization and classification, *Sedimentology* (2007), 55 (1), 31-63

[57] T. Hildebrand, P. Rüegsegger, a new method for the model-independent assessment of thickness in three-dimensional images, *journal of microscopy* (1997), 185(1), 67-75.

[58] G. Katgert, M. van Hecke, Jamming and geometry of two-dimensional foams, *EPL* (2010), 92, 34002.

[59] C. S. O'Hern, L. E. Silbert, A. J. Liu, S. R. Nagel, Jamming at zero temperature and zero applied stress : the epitome of disorder, *Phys. Rev. E* (2003), 68, 011306

[60] L. E. Silbert, A. J. Liu, S. R. Nagel, Structural signatures of the unjamming transition at zero temperature, *Phys. Rev. E* (2006), 73, 041304

[61] T. S. Majmudar, R. P. Behringer, Contact force measurements and stress-induced anisotropy in granular materials, *Nature* (2005), 435(7045):1079-82.

[62] M. van Hecke, Jamming of soft particles : geometry, mechanics, scaling and isostaticity, *J. Phys.: Condens. Matter* (2010), 22, 033101

[63] Durian 1995 : D. J. Durian, Foam mechanics at the bubble scale, *Phys. Rev. Lett.* (1995) 75, 4780

[64] M. D. Lacasse, G. S. Grest, D. Levine, Deformation of small compressed droplets, *Phys. Rev. E* (1996), 54, 5436

[65] R. Höhler, S. Cohen-Addad, Many-body interactions in soft jammed materials, *Soft Matter*, (2017), 13, 1371-1383

[66] G. Ginot, R. Höhler, S. Mariot, A. Kraynik, W. Drenckhan, Juggling bubbles in square capillaries : an experimental proof of non-pairwise bubble interactions, *Soft Matter* (2019), 15, 4570-4582

[67] D. Weaire and R. Phelan. A counter-example to Kelvin's conjecture on minimal surfaces. *Phil. Mag. Lett.* (1994), 69107–110.

[68] D. Weaire and S. Hutzler, The Physics of Foams (Oxford University Press, Oxford), (1999).

[69] C. Redenbach, Microstructure models for cellular materials, *Comput. Mater. Sci.* (2009), 44 1397–1407

[70] PJ. Steinhardt, DR. Nelson, M. Ronchetti, Bond orientational order in liquids and glasses, *Phys Rev B* (1983), 28, 784-804.

[71] W. Lechner, C. Dellago, Accurate determination of crystal structures based on averaged local bond order parameters, *J Chem Phys* (2008), 129, 114707

[72] F. Edwards, The role of entropy in the specification of a powder, In: Mehta, A. (eds) Granular Matter. (1994) Springer, New York

[73] R. L. Vink, G. T. Barkema, Configurational entropy of Network-forming materials, Phys. Rev. Lett. (2002) 89, 076405

[74] W. Voigt, Über die Beziehung zwischen den Elastizitätskonstanten isotroper, *Körper. Wied. Ann*. (1889), 38, 573–587.

[75] OE. Sotomayor, HV. Tippur, Role of cell regularity and relative density on elastoplastic compression response of 3-D open-cell foam core sandwich structure generated using Voronoi diagrams, *Acta Mater* 2014; 78:301–13.

[76] Y. Duan, B. Du, X. Zhao, N. Hou, X. Shi, B. Hou *et al.*, The cell regularity effects on the compressive responses of additively manufactured Voronoi foams. *Int J Mech Sci* (2019), 135, 105151.

[77] C. Barbier *et al*., New laws for the tension/compression properties of Voronoi closed-cell polymer foams in relation to their microstructure, *Eur. J. Mech. Solid.* (2014), 45, 110–122.

[78] X. Shi, S. Liu, H. Nie, G. Lu, Y. Li, Study of cell irregularity effects on the compression of closed-cell foams, *Int. J. Mech. Sci.* (2018), 135, 215–225

[79] HX. Zhu, JR. Hobdell, AH. Windle, Effects of cell irregularity on the elastic properties of open-cell foams. *Acta Mater* (2000), 48, 4893–900

[80] T. Miyoshi, M. Itoh, S. Akiyama, A. Kitahara, Alporas aluminum foam: Production process, properties, and application, *Adv. Eng. Mater*. (2000), 2, 179.

[81] Z. Hashin, and Shtrikman, A variational approach to the theory of the elastic behaviour of multiphase materials, *J. Mech. Phys. Solids* (1963), 11, 127–140.

[82] R. M. Christensen, Mechanics of low-density materials, *J. Mech. Phys. Solids* (1986), 34(6), 563–578.

[83] J.D. Eshelby, "The determination of the elastic field of an ellipsoidal inclusion, and related problems", *Proceedings of the Royal Society A* (1957), 241(1226): 376–396

[84] O. Zerhouni, MG Tarantino, K. Danas, Numerically-aided 3D printed random isotropic porous materials approaching the Hashin-Shtrikman bounds. *Compos Part B-Eng*(2019), 156, 344–54.

[85] MG Tarantino, O. Zerhouni, K. Danas, Random 3D-printed isotropic composites with high volume fraction of pore-like polydisperse inclusions and near-optimal elastic stiffness. *Acta Mater* (2019), 175, 331–40

[86] A. N. Gent and A. G. Thomas, Mechanics of Foamed Elastic Materials, *Rubber Chem. Technol.* (1963), 36, 597

[87] C. Redenbach, I. Shklyar, H. Andrä, Laguerre tessellations for elastic stiffness simulations of closed foams with strongly varying cell sizes. *Int. J. Eng. Sci.* (2012), 50, 70-78.

[88] Li Z, Zhang J, Fan J, Wang Z, Zhao L. On crushing response of the three-dimensional closed-cell foam based on Voronoi model, *Mech Mater* (2014), 68:85–94.

[89] Marvi-Mashhadi, M., Lopes, C. S., Llorca J., Surrogate models of the influence of the microstructure on the mechanical properties of closed-and open-cell foams. *Journal of Materials Science* (2018), 53, 12937–12948

[90] P.-Y. Lanfrey, Z. V. Kuzeljevic, M. P. Dudukovic, Tortuosity model for fixed beds randomly packed with identical particles. *Chemical Engineering Science*, (2010) 65(5), 1891 1896.

Figure_1

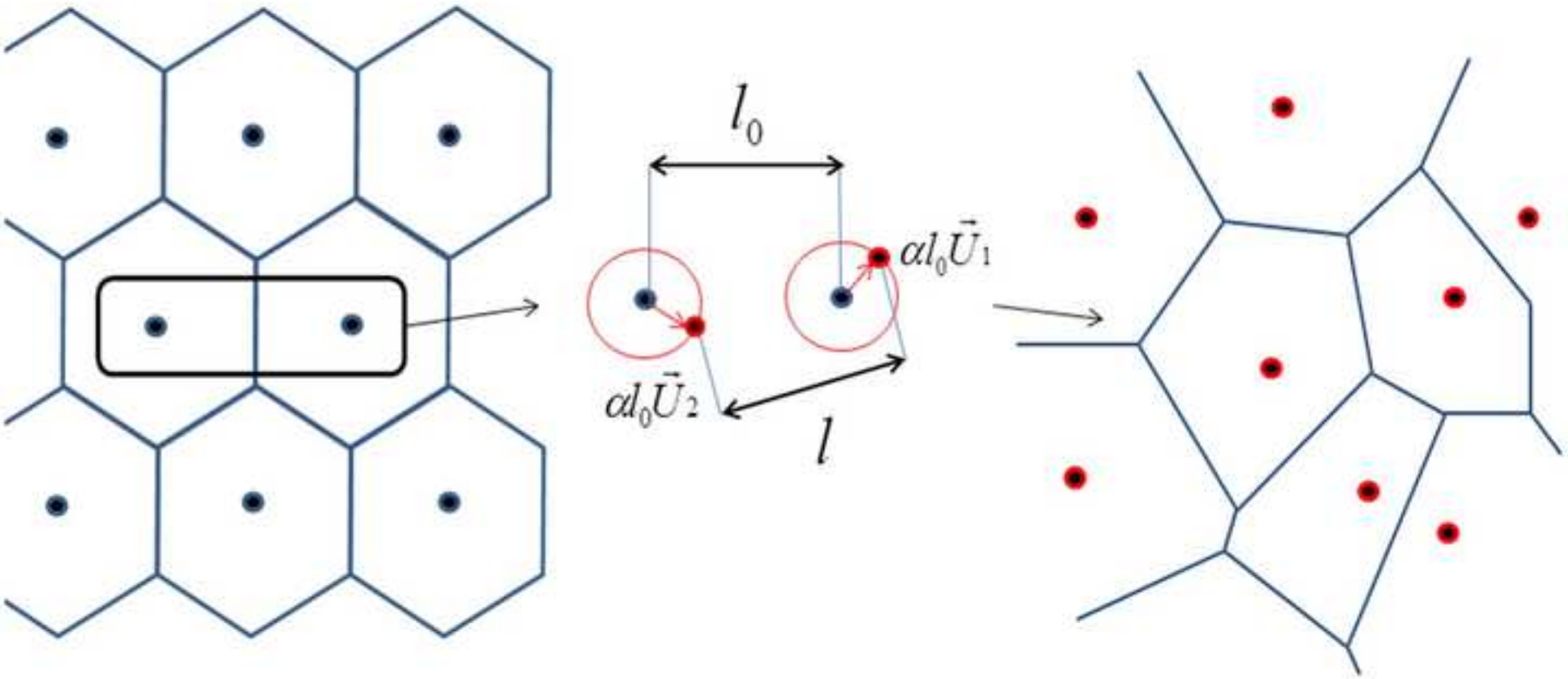

Figure_2

Click here to access/download;Figure;Figure_2.jpg

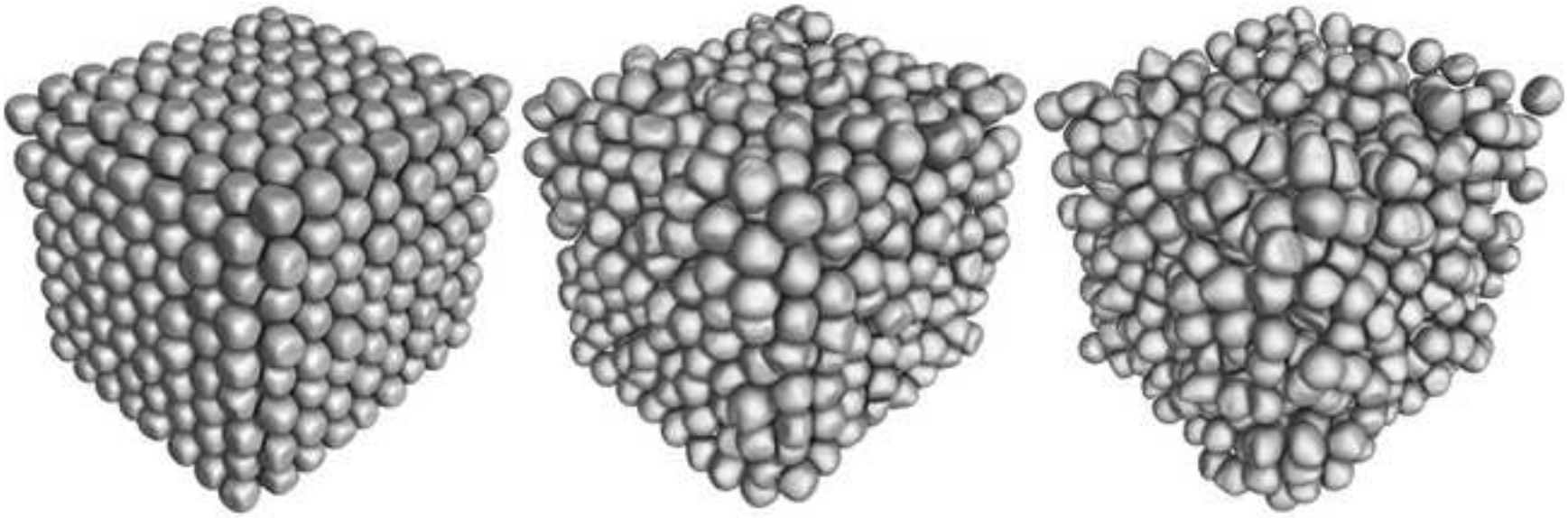

Figure_3

Click here to access/download;Figure;Figure_3.jpg

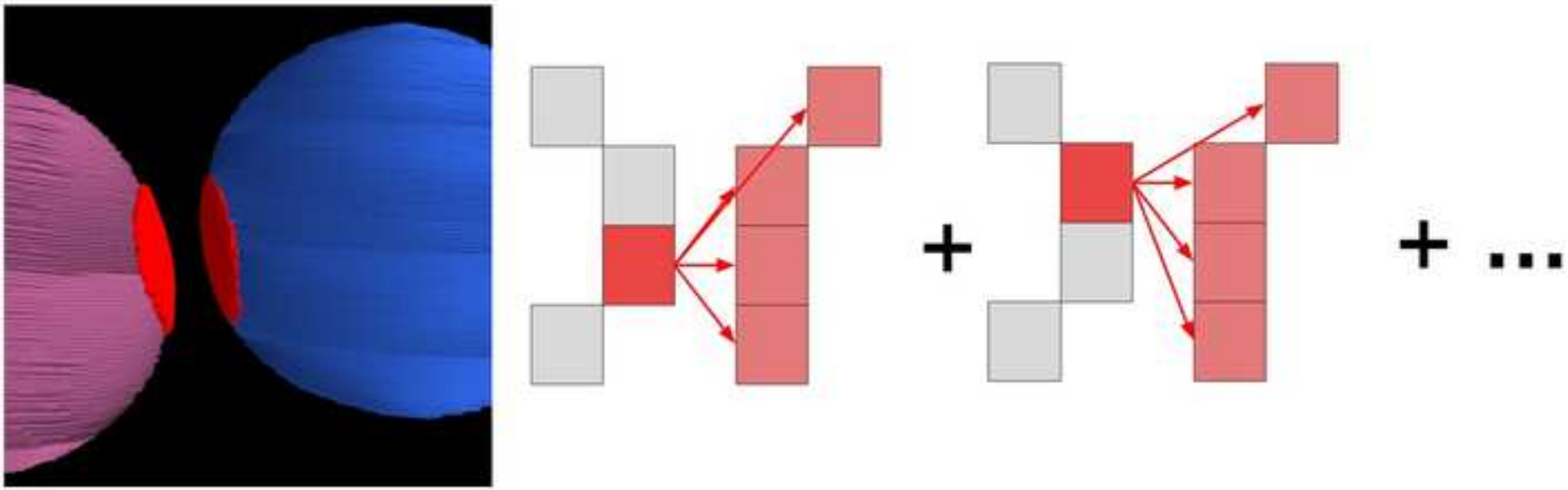

Figure_4

Click here to access/download;Figure;Figure_4.jpg

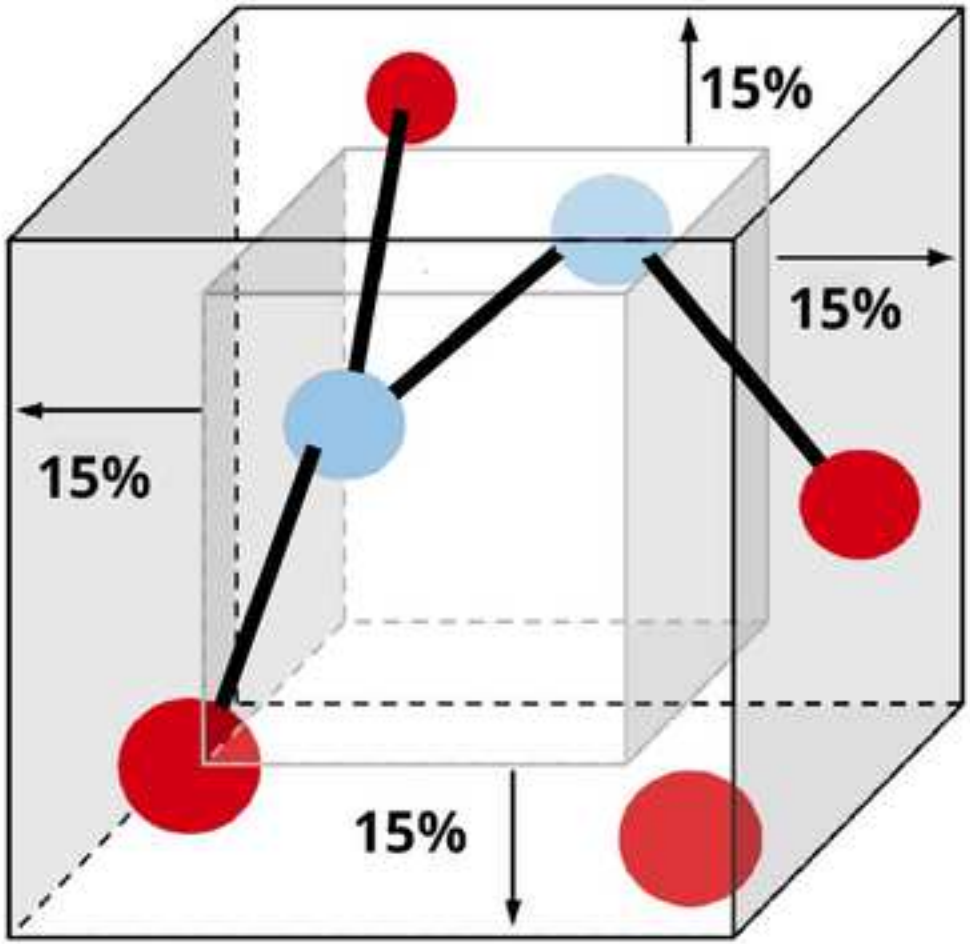

Figure_5

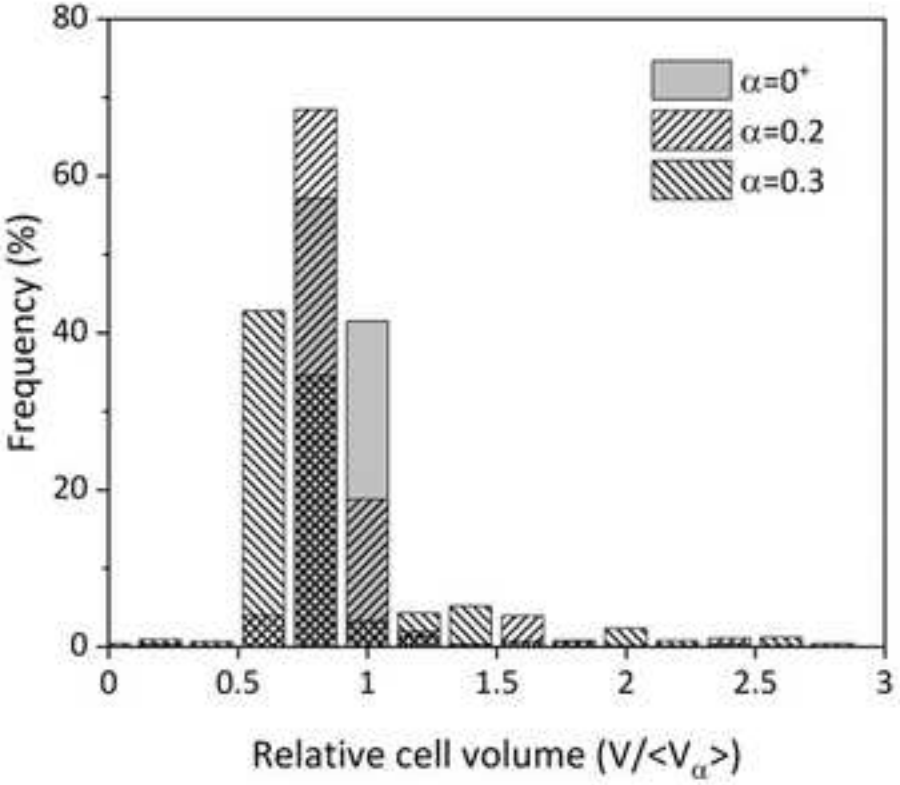

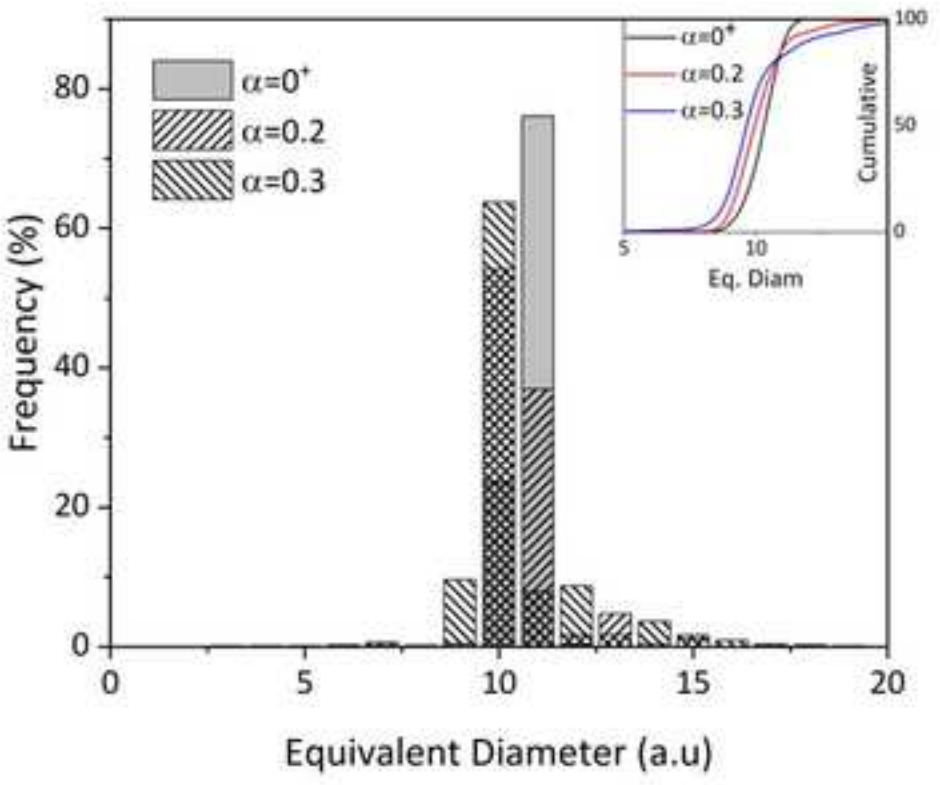

Figure_6

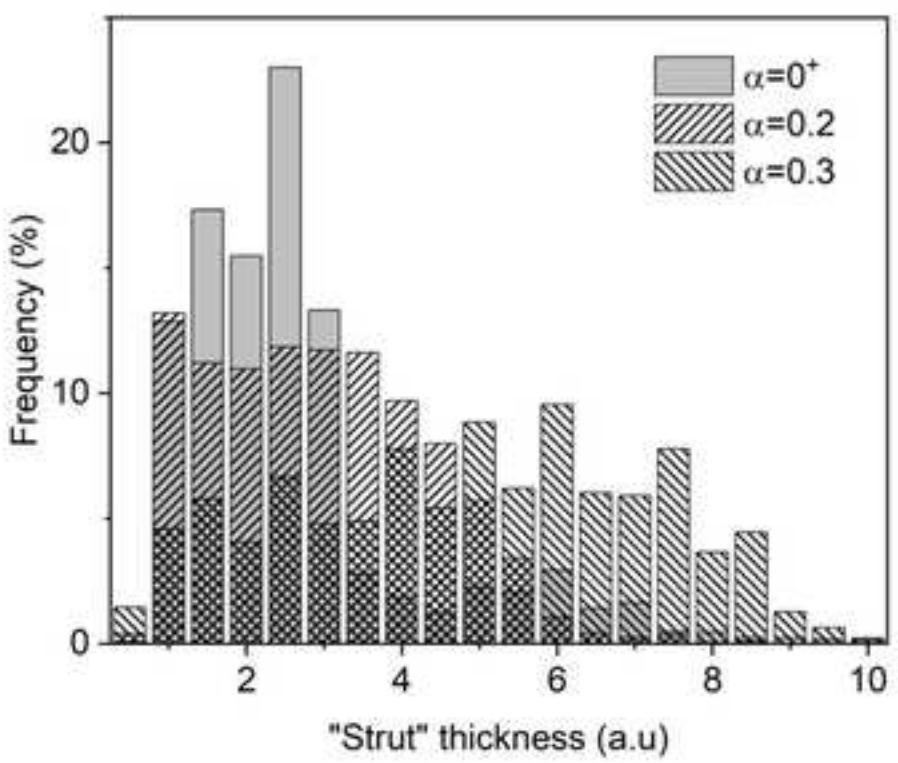

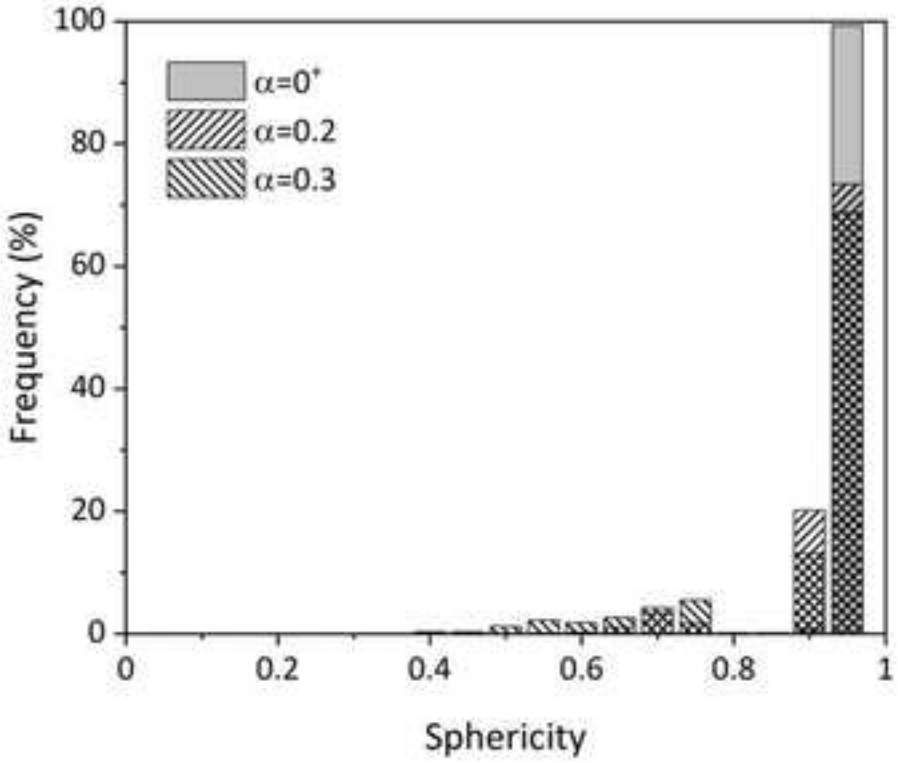

Figure_7

Click here to access/download;Figure;Figure_7.jpg

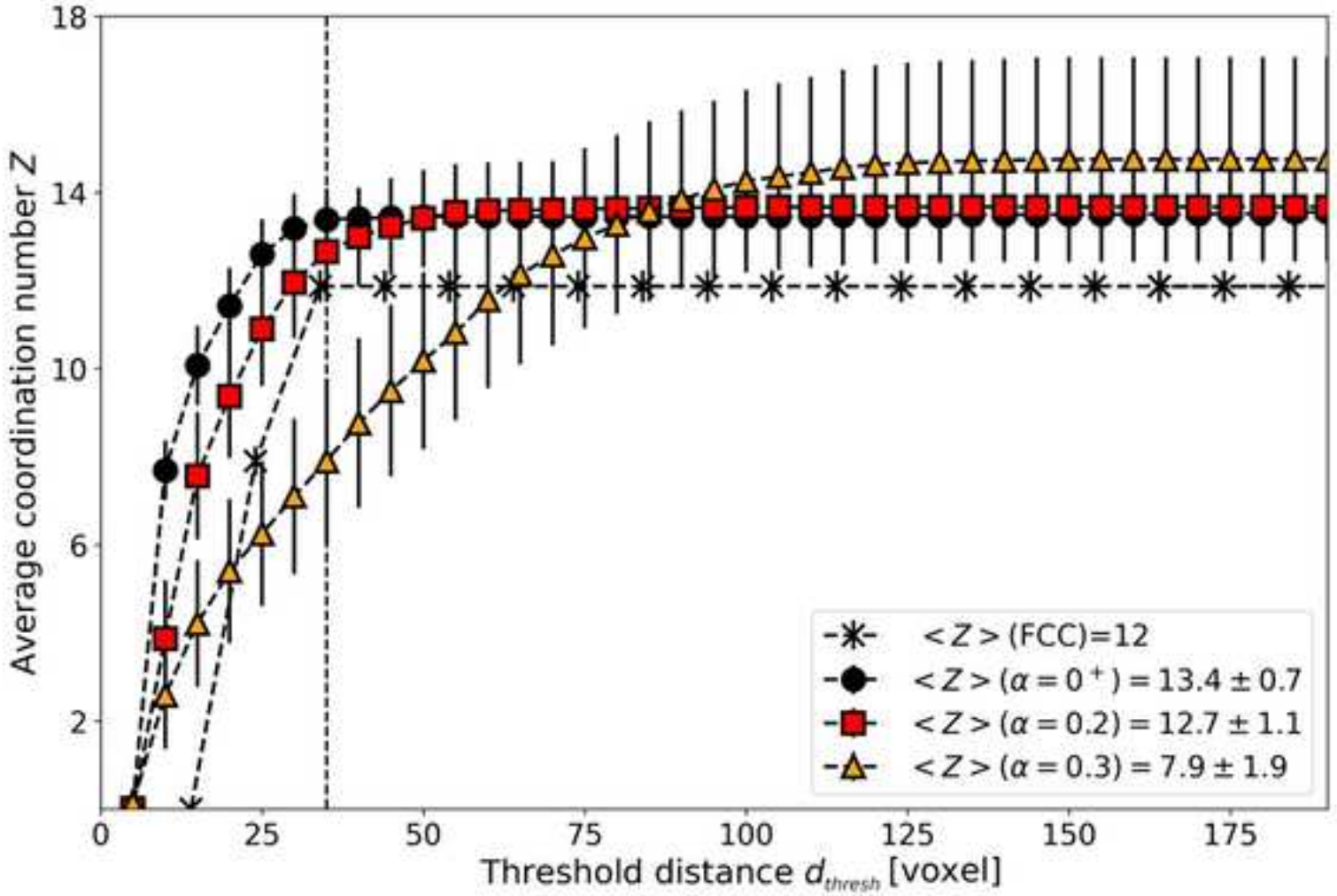

Figure_8

Click here to access/download;Figure;Figure_8.jpg

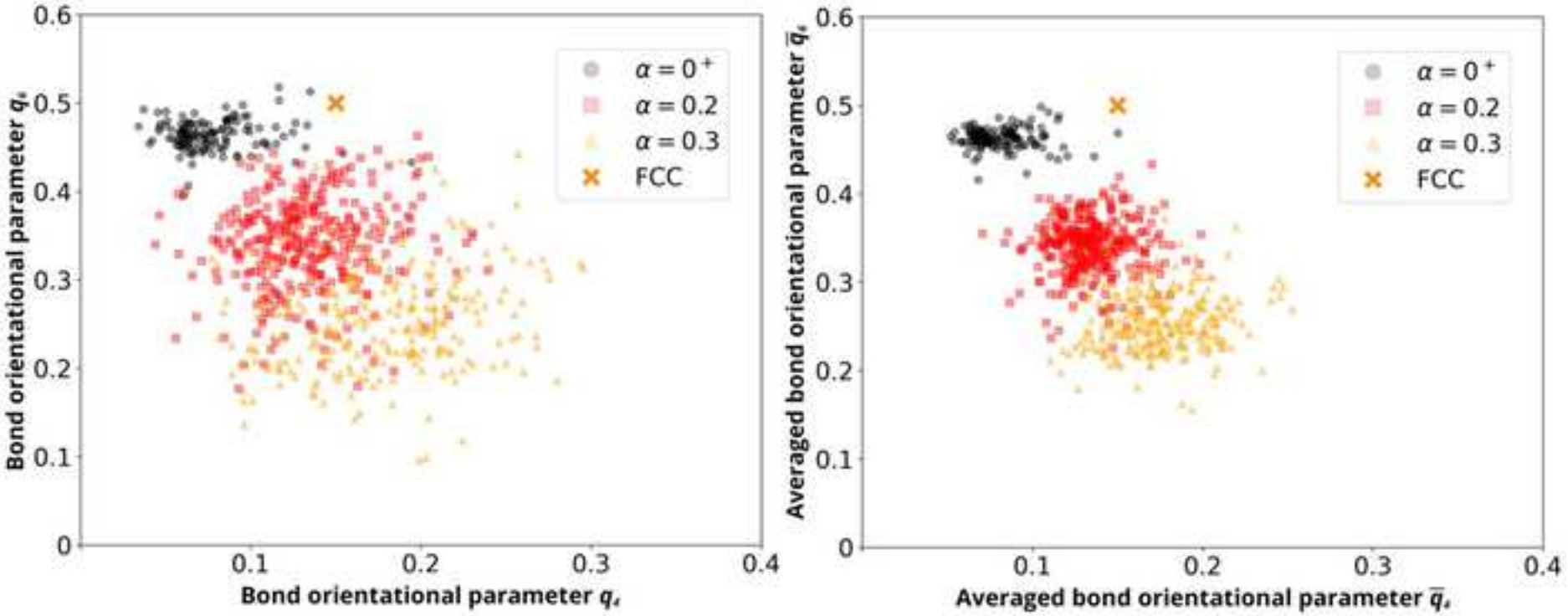

Figure_9

Click here to access/download;Figure;Figure_9.jpg

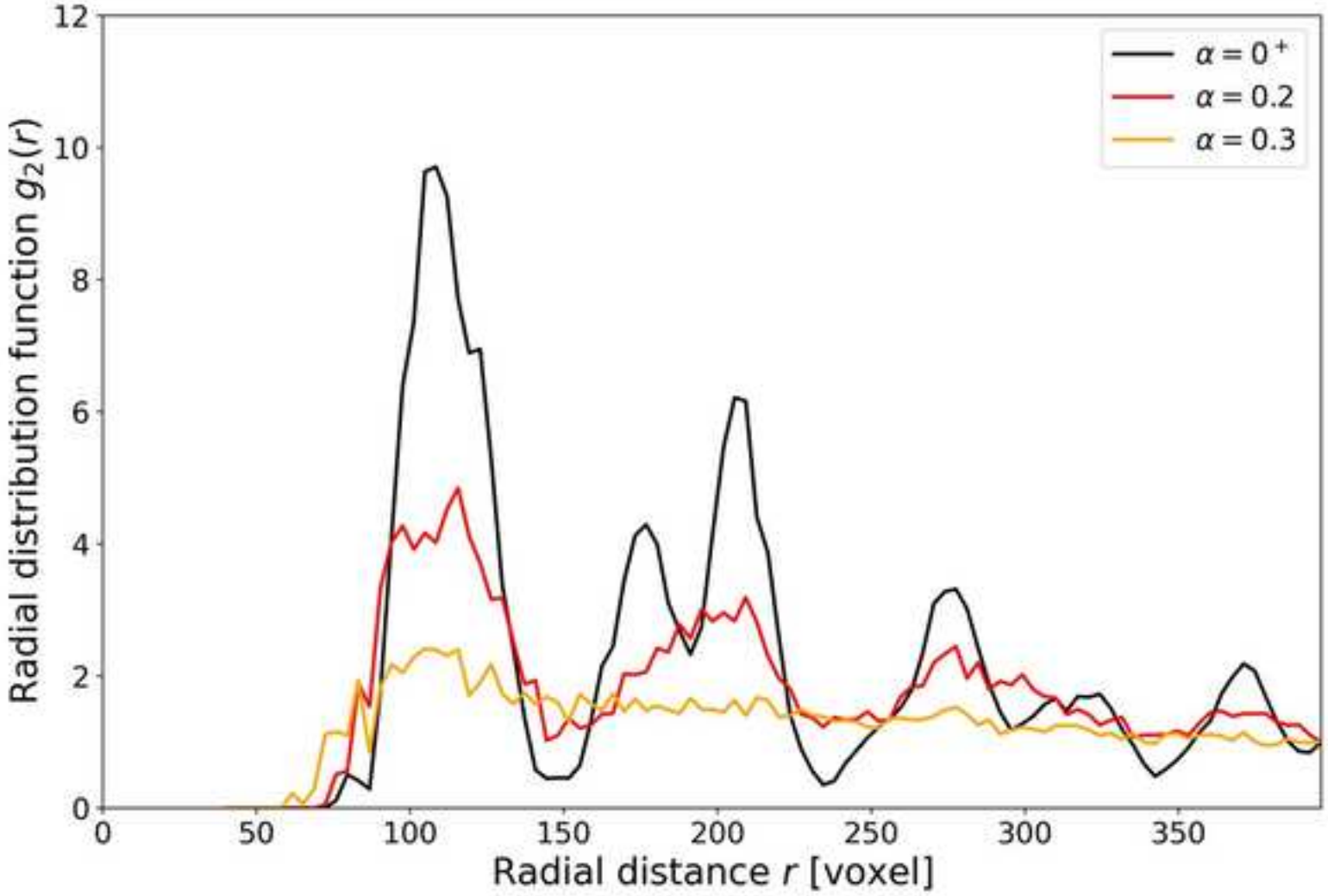

Figure_10

Click here to access/download;Figure;Figure_10.jpg

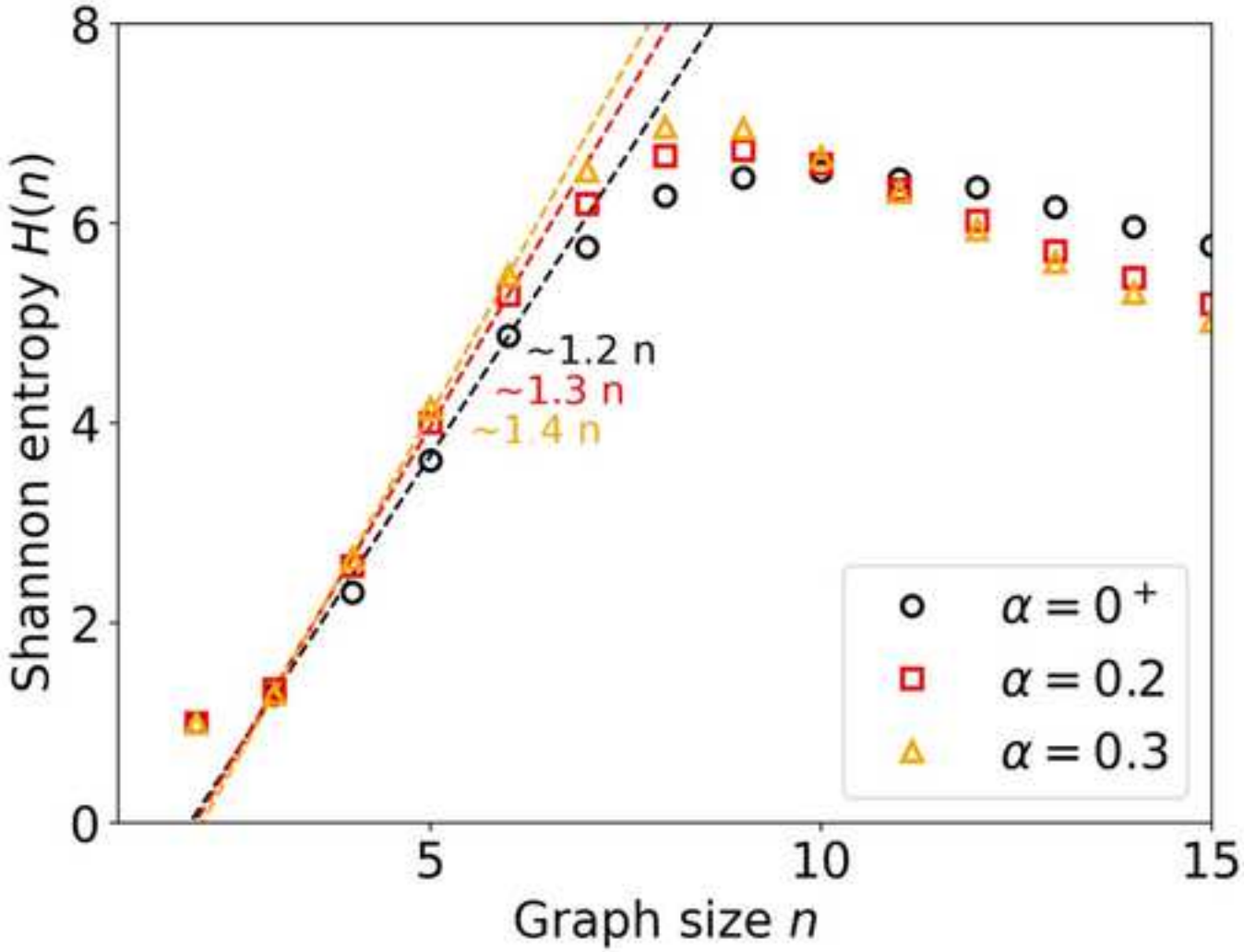

Figure_11

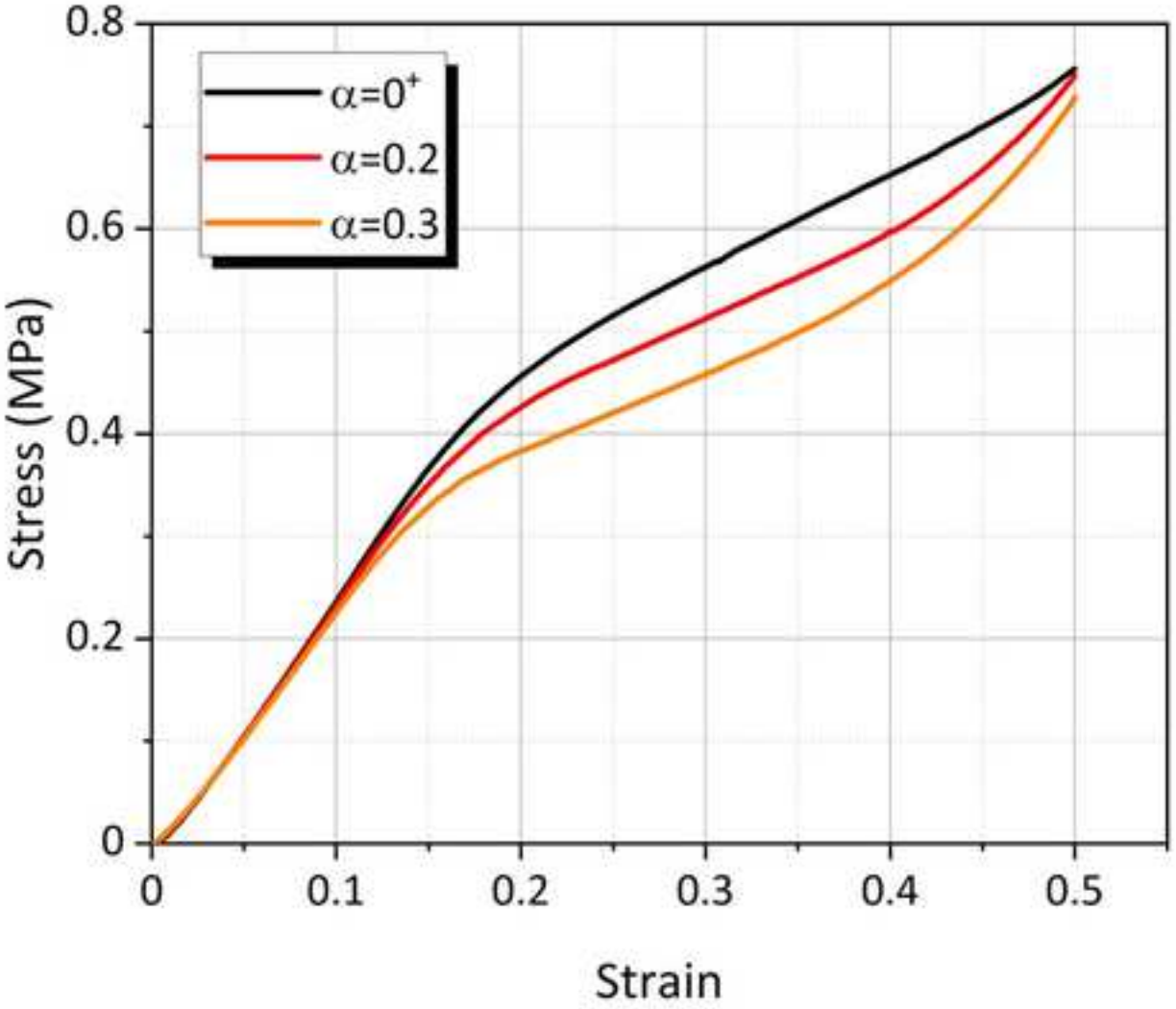

Figure_12

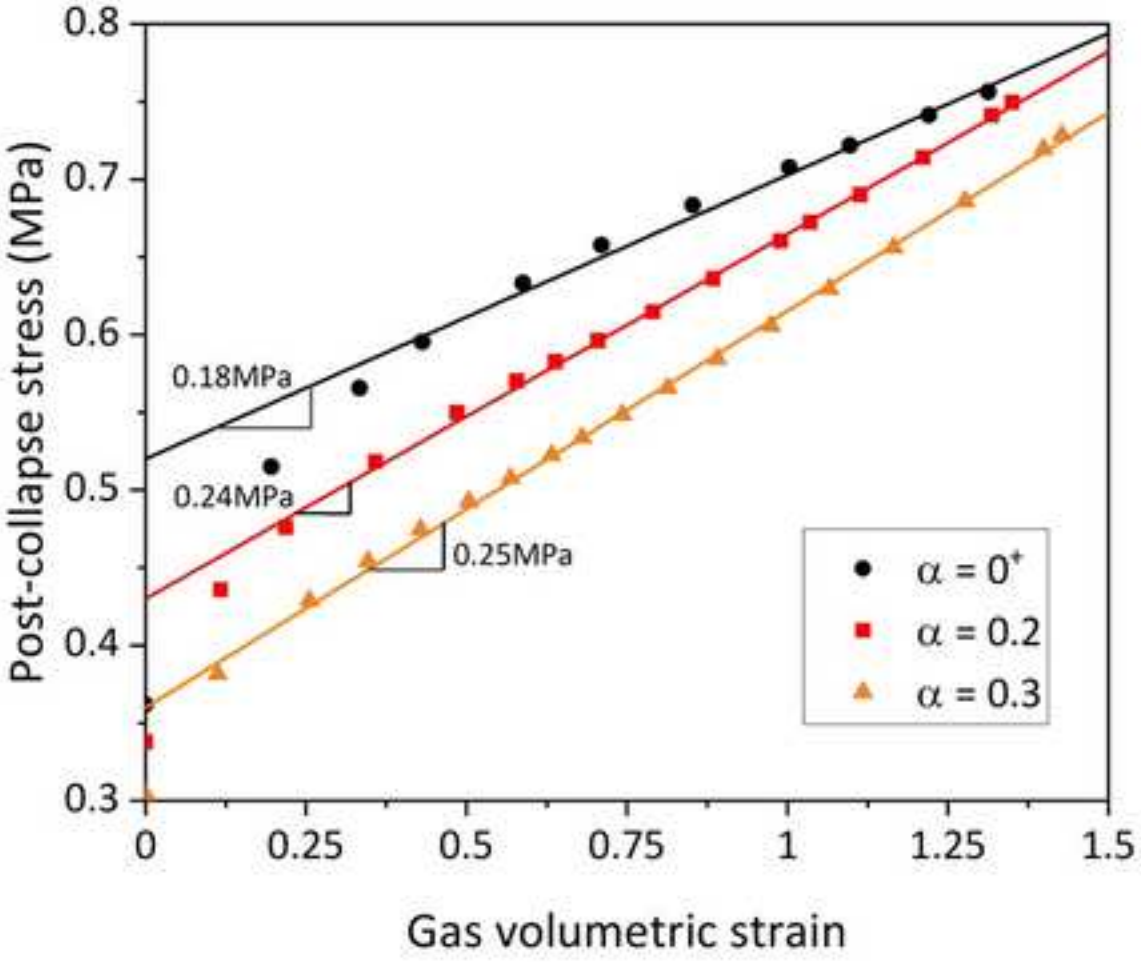

Figure_13

Click here to access/download;Figure;Figure_13.jpg

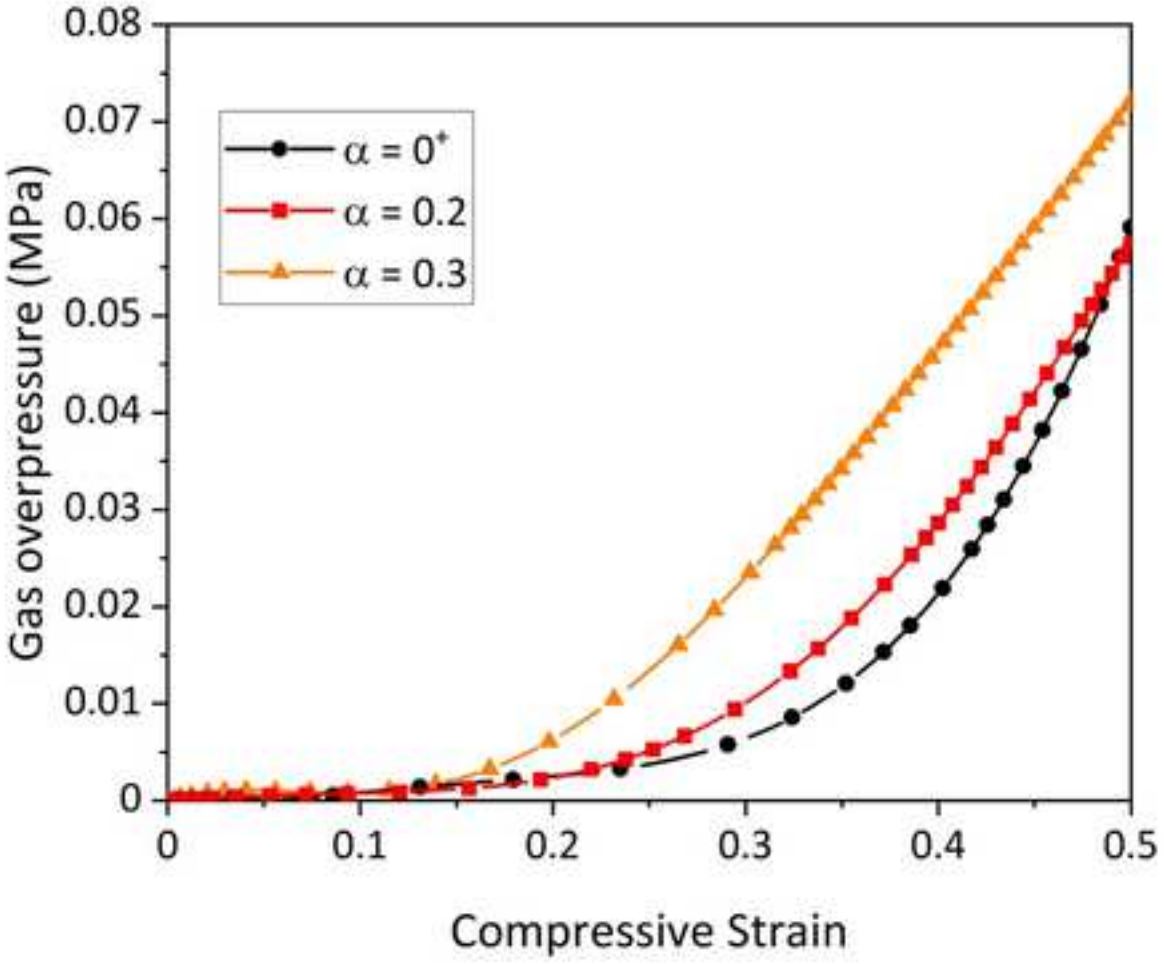

Figure_14_1

Click here to access/download;Figure;Figure_14_1.jpg

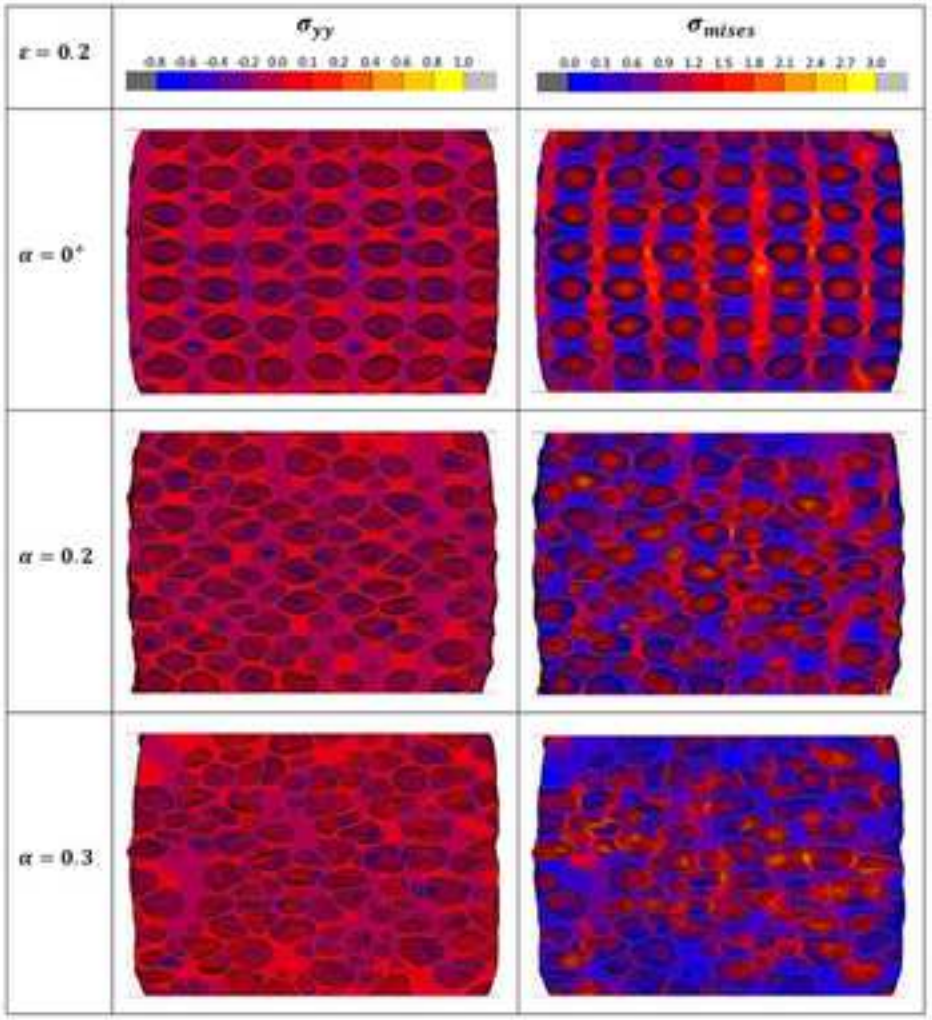

Figure_14_2

Click here to access/download;Figure;Figure_14_2.jpg

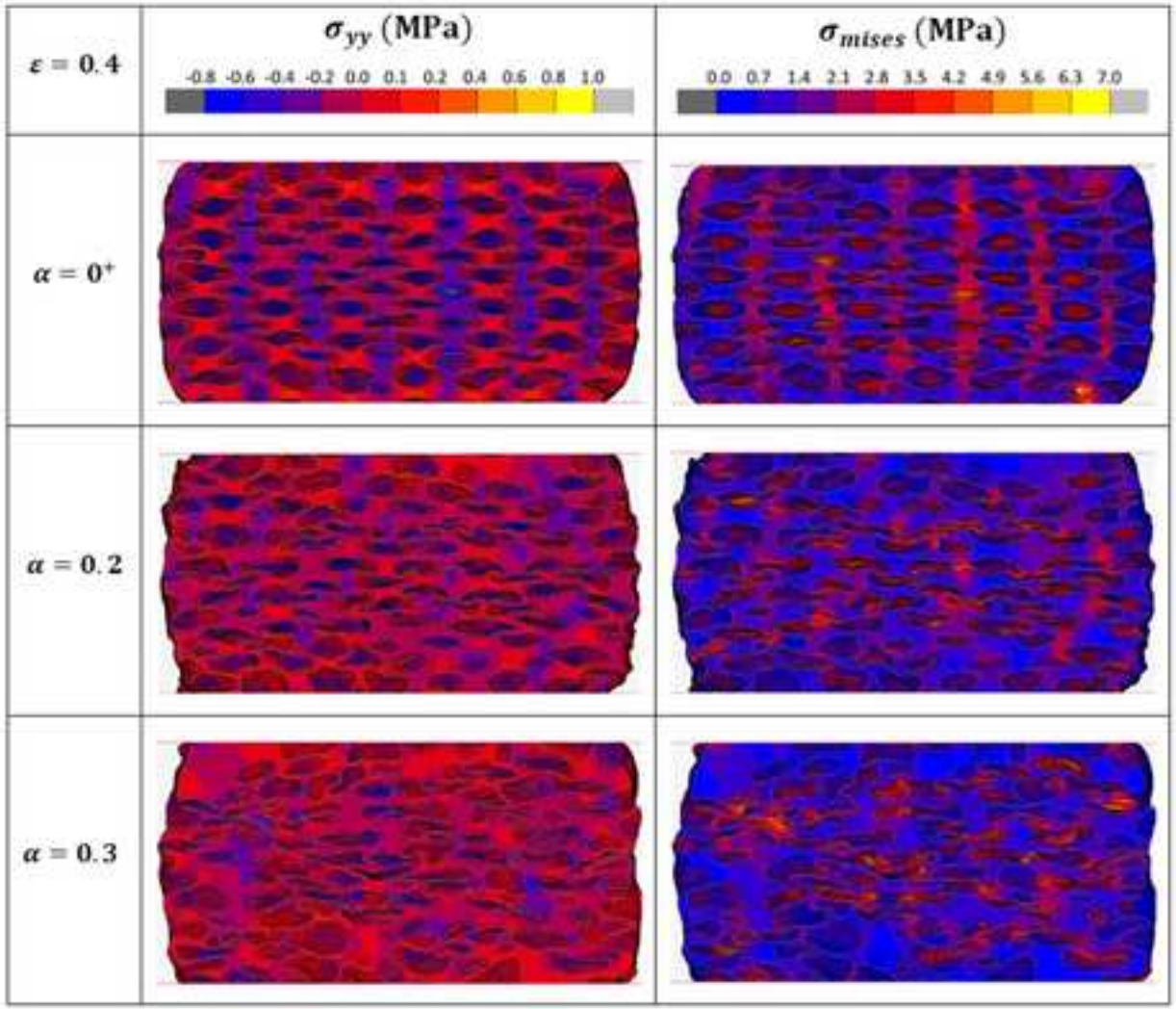

α	**0^{+}**	**0.2**	**0.3**
Porosity	0.620	0.616	0.618
$<D_{eq}>$	11.2±0.27	11.14±0.86	11.04±1.65
$<C_{vol}>$	0.07	0.28	0.59
$<S_{ph}>$	0.97	0.94	0.91
$<C_{sph}>$	$8.7.10^{-3}$	$6.4.10^{-2}$	$1.2.10^{-1}$

	Ref.	***E_f (MPa)***		***Refs.***	***E_f (MPa)***
$\frac{E_f}{E_s} = \frac{\rho_f}{\rho_s}$	[74]	3.82	$\frac{E_f}{E_s} = C_1\phi^2\left(\frac{\rho_f}{\rho_s}\right)^2 + C_2(1-\phi)\left(\frac{\rho_f}{\rho_s}\right)$	[4] [1]	1.65 1.84
$\frac{E_f}{E_s} = \frac{1}{6}\left(\frac{\rho_f}{\rho_s}\right)$	[86]	0.64	$\frac{E_f}{E_s} = \frac{\rho_f/\rho_s}{1 + C_{HS}(1-\rho_f/\rho_s)}$	[81]	2.36
$\frac{E_f}{E_s} = C_1'\left(\frac{\rho_f}{\rho_s}\right)^n$	[22] [87]	1.79 1.30	$\frac{E_f}{E_s} = \frac{2(7-5\nu_s)}{3(1-\nu_s)(9+5\nu_s)}\left(\frac{\rho_f}{\rho_s}\right)$	[82]	1.92

Eq. (6)	Eq. (7)	Eq. (8)	Present work
0.25 MPa	0.42 MPa	0.28 MPa	0.28-0.37 MPa

Declaration of interests

☒The authors declare that they have no known competing financial interests or personal relationships that could have appeared to influence the work reported in this paper.

☐The authors declare the following financial interests/personal relationships which may be considered as potential competing interests: